

# On the internal structure of starless cores. I. Physical conditions and the distribution of CO, CS, $\text{N}_2\text{H}^+$ , and $\text{NH}_3$ in L1498 and L1517B

M. Tafalla<sup>1</sup>, P.C. Myers<sup>2</sup>, P. Caselli<sup>3</sup>, and C.M. Walmsley<sup>3</sup>

<sup>1</sup> Observatorio Astronómico Nacional, Alfonso XII 3, E-28014 Madrid, Spain

<sup>2</sup> Harvard-Smithsonian Center for Astrophysics, 60 Garden St., Cambridge, MA 02138, USA

<sup>3</sup> Osservatorio Astrofisico di Arcetri, Largo E. Fermi 5, I-50125 Firenze, Italy

Received – / Accepted –

**Abstract.** We have characterized the physical structure and chemical composition of two close-to-round starless cores in Taurus-Auriga, L1498 and L1517B. Our analysis is based on high angular resolution observations in at least two transitions of  $\text{NH}_3$ ,  $\text{N}_2\text{H}^+$ , CS,  $\text{C}^{34}\text{S}$ ,  $\text{C}^{18}\text{O}$ , and  $\text{C}^{17}\text{O}$ , together with maps of the 1.2 mm continuum. For both cores, we derive radial profiles of constant temperature and constant turbulence, together with density distributions close to those of non-singular isothermal spheres. Using these physical conditions and a Monte Carlo radiative transfer model, we derive abundance profiles for all species and model the strong chemical differentiation of the core interiors. According to our models, the  $\text{NH}_3$  abundance increases toward the core centers by a factor of several ( $\approx 5$ ) while  $\text{N}_2\text{H}^+$  has a constant abundance over most of the cores. In contrast, both  $\text{C}^{18}\text{O}$  and CS (and isotopomers) are strongly depleted in the core interiors, most likely due to their freeze out onto grains at densities of a few  $10^4 \text{ cm}^{-3}$ . Concerning the kinematics of the dense gas, we find (in addition to constant turbulence) a pattern of internal motions at the level of  $0.1 \text{ km s}^{-1}$ . These motions seem correlated with asymmetries in the pattern of molecular depletion, and we interpret them as residuals of core contraction. Their distribution and size suggest that core formation occurs in a rather irregular manner and with a time scale of a Myr. A comparison of our derived core properties with those predicted by supersonic turbulence models of core formation shows that our Taurus cores are much more quiescent than representative predictions from these models. In two appendices at the end of the paper we present a simple and accurate approximation to the density profile of an isothermal (Bonnor-Ebert) sphere, and a Monte Carlo-calibrated method to derive gas kinetic temperatures using  $\text{NH}_3$  data.

**Key words.** ISM: abundances – ISM: clouds – ISM: molecules – stars: formation – ISM: individual(L1498, L1517B)

## 1. Introduction

Dense cores like those in Taurus and other nearby dark clouds represent the simplest environments where stars form. Their study holds the promise of revealing the basic physics of star formation, but despite their apparent simplicity, dense cores remain mysterious in their internal structure, formation and evolution, and in the manner in which they collapse under gravity (see, e.g., Myers 1999; Evans 1999 for recent reviews). Part of this mystery results from a number of contradictions between observations of different dense gas tracers (see, e.g., Zhou et al. 1989), which have so far precluded a self consistent description of the core internal properties. Fortunately, multi-molecular and continuum observations over the last few years have started to suggest that most contradictions arise from cores not being chemically homogeneous, as ini-

tially assumed, but having strongly differentiated interiors (Kuiper et al. 1996; Willacy et al. 1998; Kramer et al. 1999; Alves et al. 1999; Caselli et al. 1999; Bergin et al. 2001; Jessop & Ward-Thompson 2001; Tafalla et al. 2002; Bergin et al. 2002; Bacmann et al. 2002). Understanding and characterizing the chemical structure of dense cores has therefore become a top priority for star formation studies, as solving this problem may finally produce a coherent picture of dense cores, from which their star forming evolution may be inferred.

If cores have strong chemical composition gradients, in addition to density gradients, their description cannot rely on average parameters, as often assumed. It is necessary to use spatially-variable abundances, and these need to be derived from the data through a realistic modeling of the radiative transfer. This approach, unfortunately, involves a number of uncertainties, one of the largest being our ignorance of the exact (3D) geometry of a core, which is

not well constrained either by theory or 2D images (e.g., compare Jones & Basu 2002 with Curry 2002). To minimize this effect, it is convenient to concentrate on cores with relatively simple geometries, and for this reason, we have selected L1498 and L1517B as subjects of the present study.

L1498 and L1517B are two dense cores in the Taurus-Auriga cloud complex, and were first identified by Myers et al. (1983) from the inspection of Palomar Sky Atlas prints. They are not associated with IRAS point sources (Beichman et al. 1986) or 1.2 millimeter point sources (Tafalla et al. 2002), and can therefore be considered starless. Over the last decade, L1498 has been the subject of a number of detailed studies: Lemme et al. (1995) mapped its  $\text{C}^{18}\text{O}$  and CS emission, Kuiper et al. (1996) first identified it as a chemically differentiated system, and further details of its chemical structure have been presented by Wolkovitch et al. (1997) for CCS and Willacy et al. (1998) for CO. More recently, Langer & Willacy (2001) have presented an estimate of the core density profile from FIR data and Levin et al. (2001) have estimated an upper limit to its magnetic field of  $100 \mu\text{G}$  from Zeeman observations. Tafalla et al. (2002, TMCWC hereafter) presented line and continuum observations of L1498, L1517B, and three other dense cores, and found a systematic pattern of chemical differentiation: species like CS and CO are almost absent from the core interiors while  $\text{NH}_3$  and  $\text{N}_2\text{H}^+$  are present even in the densest parts. In this paper, we improve the study of L1498 and L1517B using new multiline, high angular resolution observations and creating for each core a model of the internal conditions that simultaneously explains all our  $\text{C}^{18}\text{O}$ ,  $\text{C}^{17}\text{O}$ , CS,  $\text{C}^{34}\text{S}$ ,  $\text{N}_2\text{H}^+$ , and  $\text{NH}_3$  data. As a result, we confirm the presence of a systematic abundance pattern, and show that the two cores are very close to isothermal spheres both in their density profiles and physical parameters (temperature and turbulence). At the same time, we infer that the core contraction history has been asymmetrical, both from the internal kinematics and the chemical composition. In a follow-up paper (Tafalla et al. 2004, in preparation) we will present a full chemical survey of these two cores.

## 2. Observations

We observed L1498 and L1517B in the 1.2 mm continuum with the IRAM 30m telescope in 1999 December and 2000 December. We used the MAMBO 1 bolometer array (Kreysa et al. 1998) in on-the-fly mode with a scanning speed of  $4'' \text{ s}^{-1}$ , a wobbler period of 0.5 s, and a wobbler throw of  $53''$ . The data were corrected for atmospheric extinction using sky dips done before and after each individual map, and they were reduced using the NIC software (Broguière et al. 1996). A global calibration factor of 15000 counts per Jy beam $^{-1}$  was estimated for both 1999 and 2000 epochs from observations of Uranus. The bolometer central frequency is 240 GHz and the telescope

**Table 1.** Rest Frequencies.

Line	Frequency (MHz)	Uncert. (kHz)	Ref.
$\text{C}^{18}\text{O}(J=1-0)$	109782.172	3	(1)
$\text{C}^{18}\text{O}(J=2-1)$	219560.354	1	(2)
$\text{C}^{17}\text{O}(J,F=1,7/2-0,5/2)$	112358.990	1	(3)
$\text{C}^{17}\text{O}(J,F=2,9/2-1,7/2)$	224714.214	1	(3)
CS( $J=2-1$ )	97980.953	1	(4)
CS( $J=3-2$ )	146969.026	1	(4)
$\text{C}^{34}\text{S}(J=2-1)$	96412.952	1	(4)
$\text{C}^{34}\text{S}(J=3-2)$	144617.101	1	(4)
$\text{NH}_3(\text{JKF}_1\text{F}=1110.5-1111.5)$	23694.501	0.1	(5)
$\text{N}_2\text{H}^+(\text{JF}_1\text{F}=101-021)$	93176.258	10	(6)
$\text{N}_2\text{H}^+(\text{JF}_1\text{F}=344-233)$	279511.811	6	(7)

References: (1) C. Gottlieb, priv. comm.; (2) Müller et al. (2001); (3) Cazzoli et al. (2002); (4) Gottlieb et al. (2003); (5) Kukolich (1967); (6) Lee et al. (2001), astronomical; (7) Caselli et al. (2002c), astronomical

beam size is approximately  $11''$ . (The 1999 data have already been presented in Tafalla et al. 2002.)

We observed L1498 and L1517B in  $\text{C}^{18}\text{O}(1-0)$ ,  $\text{C}^{18}\text{O}(2-1)$ ,  $\text{C}^{17}\text{O}(2-1)$ , CS( $2-1$ ), CS( $3-2$ ),  $\text{C}^{34}\text{S}(2-1)$ ,  $\text{C}^{34}\text{S}(3-2)$ , and  $\text{N}_2\text{H}^+(1-0)$  with the IRAM 30m telescope in 2000 October. L1498 was mapped in all lines and L1517B was mapped in all but  $\text{C}^{34}\text{S}(2-1)$  and  $\text{C}^{34}\text{S}(3-2)$ , which were so weak that only the central position was observed. Additional  $\text{N}_2\text{H}^+(3-2)$  observations were carried out in 2001 April. All data were taken in frequency switching mode with frequency throws of approximately 7 or 14 MHz. As a backend we used the facility autocorrelator, split into several windows to achieve velocity resolutions between  $0.03$  and  $0.06 \text{ km s}^{-1}$ . The telescope pointing was corrected using frequent cross scans of continuum sources, and the total errors were found to be smaller than  $4''$  (rms). The data were calibrated using the standard chopper wheel method and converted to the main beam brightness temperature scale. The full width at half maximum (FWHM) of the telescope beam is inversely proportional to the frequency, and ranges from approximately  $26''$  at the (lowest) frequency of  $\text{N}_2\text{H}^+(1-0)$  to  $11''$  at the (highest) frequency of  $\text{N}_2\text{H}^+(3-2)$ .

As stressed in previous studies (Lee et al. 2001; Tafalla et al. 2002), the modeling and interpretation of the very narrow spectral lines from starless cores like L1498 and L1517B (FWHM  $\approx 0.2 \text{ km s}^{-1} \approx 70 \text{ kHz}$  at 100 GHz) requires using rest frequency values more accurate than those in standard compilations. Fortunately, current laboratory work is starting to produce frequency determinations with uncertainties of the order of 1 kHz, and whenever such a measurement exists we have preferred it over any other value, including our own previous astronomical determinations (Lee et al. 2001). The rest frequencies used in this paper are indicated in Table 1.

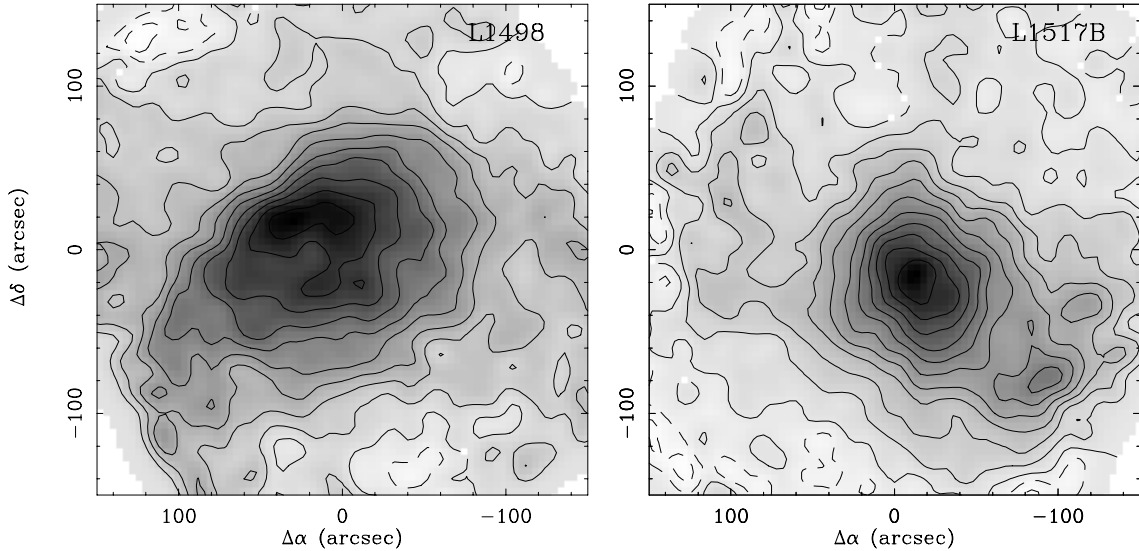


**Fig. 1.** 1.2 mm continuum maps of L1498 (left) and L1517B (right). Note the central concentration and symmetry of the emission. In order to enhance the sensitivity, each map has been convolved with a 20'' gaussian. First contour and contour spacing are 2 mJy/11''-beam, and central coordinates are ( $\alpha_{1950} = 4^h 7^m 50^s.0$ ,  $\delta_{1950} = 25^{\circ} 02' 13''$ ) for L1498 and ( $\alpha_{1950} = 4^h 52^m 7^s.2$ ,  $\delta_{1950} = 30^{\circ} 33' 18''$ ) for L1517B.

### 3. Results

#### 3.1. Continuum data and density profiles

In contrast with the molecules, whose emissivity is highly sensitive to excitation and chemistry (see below), the dust in a starless core is expected to have an emissivity approximately constant with radius (see also below for caveats). This property allows a rather straightforward conversion of the observed continuum emission into a density profile (e.g., Ward-Thompson et al. 1994; André et al. 1996; Evans et al. 2001), and for this reason, we start our analysis of L1498 and L1517B by studying their dust emission.

Figure 1 presents 1.2 mm continuum maps of L1498 and L1517B, and shows that in both cores the mm emission is centrally concentrated. In L1498, the emission appears slightly elongated SE-NW, while L1517B is rounder with a weak extension to the SW (and a weaker one to the NE). Neither of the cores presents evidence for an unresolved point-like component, indicative of an embedded object, so they appear as bona fide starless cores.

To estimate the density distributions of L1498 and L1517B from the data shown in Fig. 1, we follow the same procedure as in TMCWC (where the December 1999 part of this dataset was presented). Thus, we approximate each core as a spherical system, and derive a continuum radial profile by taking an azimuthal average of its map. As L1498 is slightly elongated, we average the data of this source in ellipses of position angle  $-40^{\circ}$  and aspect ratio  $b/a = 0.6$ , while for the rounder L1517B, we average the data in circles. These radial profiles are presented in Fig. 2 both in linear and log-log scales. (Core centers are assumed to be at  $(10'', 0)$  and  $(-15'', -15'')$  for L1498 and L1517B, respectively.)

To model each continuum radial profile we need to assume a dust temperature law. Theoretical models of the dust temperature in cores predict a slight inward decrease (Mathis et al. 1983; Evans et al. 2001; Zucconi et al. 2001), which for the case of the L1498 and L1517B cores is estimated to range between 11 K in the outer layers and 8 K in the innermost part (Evans et al. 2001, their model for L1512). Here, for simplicity (and from our  $\text{NH}_3$  analysis in Section 3.3), we will assume that both cores have a constant dust temperature of 10 K, and we will use this value to estimate their density radial profiles (see also Langer & Willacy 2001).

In addition, we assume a constant dust emissivity of  $\kappa_{1.2mm} = 0.005 \text{ cm}^2 \text{ g}^{-1}$ , for consistency with previous work (e.g., André et al. 1996). Following TMCWC, we fit the data using a density profile of the form

$$n(r) = \frac{n_0}{1 + (r/r_0)^{\alpha}},$$

where  $n_0$  is the central density,  $r_0$  is the radius of the inner “flat” region ( $2r_0$  is the full width at half maximum), and  $\alpha$  is the asymptotic power index. For each choice of  $n_0$ ,  $r_0$ , and  $\alpha$ , we calculate the emergent continuum distribution by integrating the equation of radiative transfer in the optically thin case, and simulate an on-the-fly bolometer observation of such a distribution using the same instrumental parameters as those used at the telescope. The radial profile of this simulated observation is compared with the measured radial profile, and the free parameters  $n_0$ ,  $r_0$ , and  $\alpha$  are modified until model and data agree. As shown by the solid lines in Fig. 2, the final choice of free parameters (Table 2) gives very reasonable fits for both cores, and indicates that L1517B is twice as dense at its center than L1498, while it has a FWHM approximately

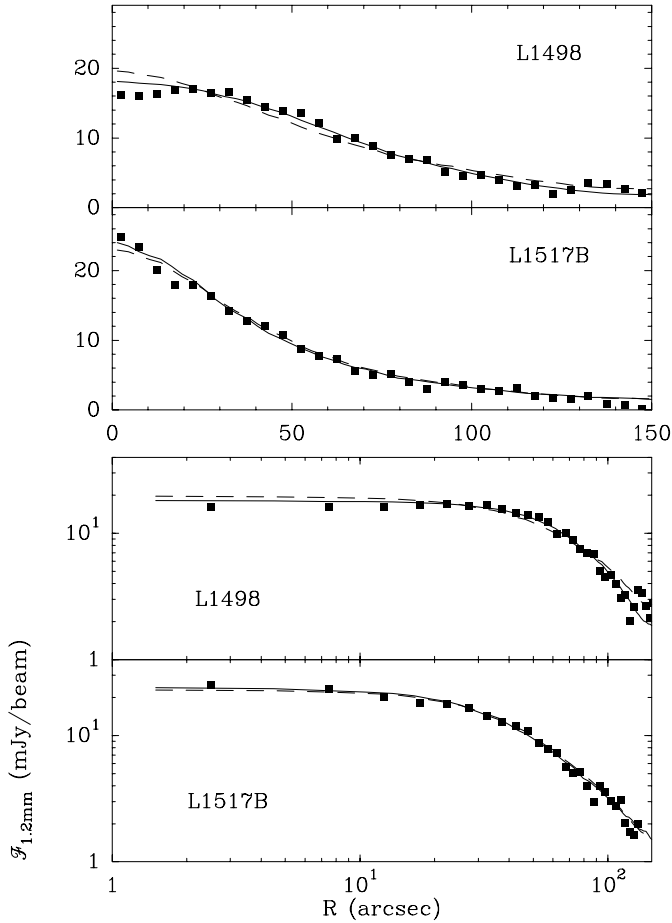


**Fig. 2.** Radial profiles of 1.2 mm continuum emission (from the maps in Fig. 1). The squares represent observed data and the lines are the predictions from two density models: the solid line is a simple analytic model and the dashed line is an isothermal model (see text). Both linear-linear and log-log plots are shown.

half that of L1498 (so both cores have similar central column densities:  $3\text{--}4 \times 10^{22} \text{ cm}^{-2}$ ). We note that the fit for L1517B is the same as derived in TMCWC, while the fit for L1498 is only slightly different (by less than 10% for radii smaller than 110'' and by less than 30% in the range 110–150'').

Although our analytical density distributions accurately fit the continuum data, their motivation is purely phenomenological. As detailed in Appendix A, however, a particular choice of parameters in this density family provides an excellent approximation to an isothermal function (or Bonnor-Ebert sphere), and this choice happens to be the best fit for L1517B (see Appendix A for further details). This “coincidence” motivated us to explore isothermal fits to the L1517B and L1498 radial profiles as an alternative to the analytical models presented before. For this, we have used the numerical solution to the isothermal function by Chandrasekhar & Wares (1949), and searched for the best fit to each core by varying the central density and the isothermal sound speed as independent free parameters. In this procedure, we have fol-

**Table 2.** Density fits from continuum data

	Analytic <sup>(a)</sup>			Isothermal	
	$n_0$ (cm $^{-3}$ )	$r_0$ (")	$\alpha$	$n_0$ (cm $^{-3}$ )	$a$ (km s $^{-1}$ )
L1498	$0.94 \times 10^5$	75	3.5	$1.35 \times 10^5$	0.32
L1517B	$2.2 \times 10^5$	35	2.5	$2.2 \times 10^5$	0.27

<sup>a</sup>  $n(r) = n_0 / (1 + (r/r_0)^\alpha)$

lowed the steps explained in the fitting with analytical models including the on-the-fly simulation, and the best fit parameters are given in Table 2. As can be seen in Fig. 2, the isothermal models (dashed lines) provide reasonable fits to the observed continuum data, especially for the rounder L1517B, where the isothermal and analytic models are indistinguishable (see also Appendix A). For the more elongated L1498 core, the isothermal model does not fit the radial profile as well as the analytic function, but its deviation from the data is never very large ( $\sim 25\%$  at the center), and is less than the deviation of this core from spherical geometry (about 40%). Our fits of L1498 and L1517B, therefore, add to recent evidence that the density profiles of starless cores can be modeled exactly or approximately by isothermal spheres (Bacmann et al. 2000; Alves et al. 2001; Evans et al. 2001).

As shown by Ebert (1955) and Bonnor (1956), a self gravitating isothermal sphere is stable only if it is bounded from the outside and its center-to-edge density contrast does not exceed a limiting value close to 14, or equivalently, its dimensionless radius ( $\xi$ ) does not exceed the critical value 6.45. Although neither L1498 nor L1517B show a clear boundary at which the core merges with an external medium, we can assess possible core stability by calculating the critical radius for each core. For the less centrally concentrated L1498 core, the critical radius occurs at 150'', which is at the very edge of our map (defined by the sensitivity of our continuum measurements). For L1517B, the critical radius occurs at 100''; so if the isothermal core continues to the edge of our map, the core would seem unstable. This situation is similar to that found by Bacmann et al. (2000) in their study of a sample of starless cores with ISOCAM. We defer further discussion of the isothermal model and its stability to section 4.1.

### 3.2. Overview of the molecular line data and model parameters

To derive the temperature, kinematics, and chemical structure of L1498 and L1517B, we now analyze their molecular emission. Before starting the detailed radiative transfer modeling, we first present a comparison between the integrated maps of all species and identify the most general trends. As Figure 3 shows (see also TMCWC), the maps of each core display a striking dichotomy—almost to the point of anti correlation—between the distribution of the different tracers: the 1.2 mm continuum, N<sub>2</sub>H<sup>+</sup>, and

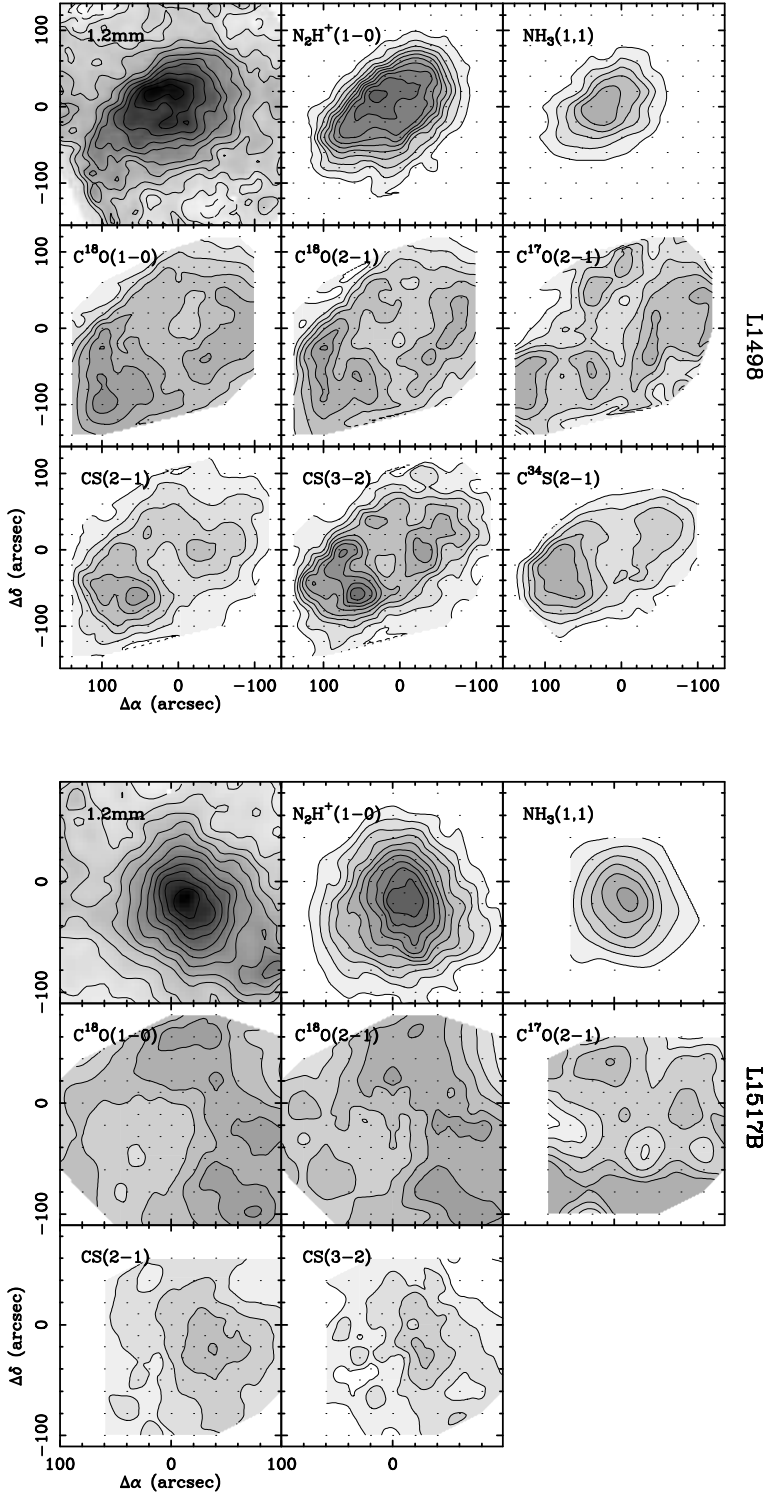


**Fig. 3.** Integrated intensity maps for continuum and lines observed toward L1498 and L1517B. Note the systematic dichotomy between centrally-peaked and centrally-depressed morphologies. For each core, the top row shows the maps of centrally-peaked tracers, 1.2 mm continuum,  $\text{N}_2\text{H}^+$ , and  $\text{NH}_3$ , and the two lower rows present the maps of centrally-depressed species, isotopomers of CO (middle row) and isotopomers of CS (bottom row). In each map, the lowest contour and the contour interval are equal, and for each line, the same contour choice has been used for both L1498 and L1517B. Lowest contours are (in  $\text{K km s}^{-1}$ ): 0.15 for  $\text{C}^{18}\text{O}(1-0)$  and  $(2-1)$ , 0.05 for  $\text{C}^{17}\text{O}(2-1)$ , 0.25 for  $\text{N}_2\text{H}^+(1-0)$ , 1.5 for  $\text{NH}_3(1,1)$ , 0.15 for  $\text{CS}(2-1)$ , 0.1 for  $\text{CS}(3-2)$ , and 0.05 for  $\text{C}^{34}\text{S}(2-1)$ . Continuum maps and central positions as in Fig. 1. The  $\text{C}^{17}\text{O}(2-1)$  data have been convolved with a  $35''$  (FWHM) gaussian to improve S/N.

$\text{NH}_3$  emission on the one hand are compact and centrally concentrated, while the CO and CS isotopomer emission on the other hand are extended and almost ring-like. In the larger L1498 core, the CO/CS ring is well resolved spatially, and it appears fragmented with a bright peak toward the SE. In the more compact L1517B core, the CO isotopomers form a well-defined half ring toward the west, while the CS emission is more concentrated, although it is still offset toward the west from the  $1.2 \text{ mm}/\text{N}_2\text{H}^+$  maximum.

As modeled in detail in the next sections, the ring distributions of the CO and CS isotopomers result from a sharp drop in the abundances of these molecules toward the dense centers of the cores, most likely caused by the freeze out of these molecules onto dust grains (for additional cases, see Kuiper et al. 1996; Willacy et al. 1998; Kramer et al. 1999; Alves et al. 1999; Caselli et al. 1999; Bergin et al. 2001; Jessop & Ward-Thompson 2001; Bacmann et al. 2002; TMCWC).  $\text{N}_2\text{H}^+$  and  $\text{NH}_3$ , on the other hand, seem immune to this process at typical core densities and they are present in the gas phase all throughout the core.

The goal of the following sections is to derive self consistent models of the internal structure of L1498 and L1517B that fit simultaneously all line observations. For this, we model the cores as spherically symmetric systems and predict the emission from each molecule with a Monte Carlo radiative transfer code based on that of Bernes (1979). The physical properties of these models are fully defined by radial profiles of density, temperature, turbulent velocity, and systematic velocity, and the same parameters are used to model all molecular lines. As core density profiles, we use the analytic functions derived from the continuum data, and the rest of the gas parameters are derived from the molecular line data. In our derivation of these parameters we have favored simplicity over detailed fine tuning, and here we summarize the main results (see following sections for more details and Table 3 for a parameter list). To derive gas temperature profiles, we have used the  $\text{NH}_3$  data, and we have found that this parameter is constant with radius in both cores (section 3.3). The turbulent profiles are also derived from the  $\text{NH}_3$  data, and they are constant with radius, as indicated by the radial profiles of linewidth (section 3.7.1). The profiles of systematic velocity have been derived from the combined fit to all line shapes, as different species trace the gas velocity at different radii depending on optical depth. For both L1498 and L1517B, we find that the velocity field in the core central part is constant, as indicated by the  $\text{NH}_3$  data, and that there is a slight gradient toward the outside traced by the velocity of the CS self absorptions (section 3.6). For simplicity we have modeled this outer gradient with a linear function.

When modeling the self absorbed lines of CS (section 3.6),  $\text{HCO}^+$ , and HCN (Tafalla et al. 2004 in preparation), the shape of the profiles depends very sensitively on the gas conditions at very large radii ( $> 4 \times 10^{17} \text{ cm} \approx 190''$ ). These conditions, however, cannot be safely extrapolated

from our dust continuum or  $\text{NH}_3$  data, as they correspond more to the ambient cloud or envelope than to the dense core itself, and favoring again simplicity, we have modeled them using constant gas parameters determined from an approximate fit to the line self absorptions of different molecules. For both L1498 and L1517B, we have introduced a discontinuity in the density profile at  $4 \times 10^{17} \text{ cm}$ , where both cores reach a density of approximately  $3 \times 10^3 \text{ cm}^{-3}$ , and we have extended these profiles with envelopes of constant density equal to  $10^3 \text{ cm}^{-3}$  up to a radius of  $8 \times 10^{17} \text{ cm}$ . To match the self absorption features, we have set the velocity of this envelope equal to zero for L1517B and to  $0.35 \text{ km s}^{-1}$  for L1498 (inward motion), and the turbulent component equal to 4 and 5 times the central turbulence, for L1517B and L1498 respectively. As we will see below, the inward-moving envelope component in L1498 seems only present in the front part of the cloud and most likely represents an unrelated foreground cloud, so we have neglected the contribution of the back side of the envelope in this object. It should be stressed that our parameterization of the cloud envelopes is highly simplified and it has been carried out with the only purpose of fitting the shape of the self absorbed lines. These envelopes have no effect on the emission of the thin lines used to determine the abundance profiles of each species, so their role in the modeling is almost cosmetic. Detailed mapping of the environment surrounding the cores is necessary to further constrain the envelope properties.

Having fixed the physical parameters of the cores (summarized in Table 3), the only free parameter left to fit the emission of each species is the radial profile of its abundance. To determine this profile, we have searched for Monte Carlo solutions of the radiative transfer that fit simultaneously the radial profile of integrated intensity and the central spectrum of each observed transition. This approach is similar to that of TMCWC, with the novelty that the present analysis uses higher spatial resolution observations, and that for each species we simultaneously model multiple transitions. This new analysis results in a more detailed and accurate derivation of the physical and chemical structure of the cores.

### 3.3. $\text{NH}_3$ : constant temperature and central abundance enhancement

TMCWC used  $\text{NH}_3$  data to determine the gas kinetic temperature of several cores including L1498 and L1517B. Given the importance of this parameter and the recent calculations of the expected temperature structure of dense cores (Evans et al. 2001; Zucconi et al. 2001; Galli et al. 2002), here we present an improved  $\text{NH}_3$  analysis using the new density profiles of section 3.1 and a more accurate temperature determination method. Our new method is an updated version of the classical analysis (e.g., Walmsley & Ungerechts 1983) calibrated with Monte Carlo radiative transfer models, and as detailed in Appendix B, it provides accurate temperature determina-

**Table 3.** Monte Carlo model fits

Parameter	L1498	L1517B	Note
Core			
$r_{max}$ (cm)	$4 \times 10^{17}$	$4 \times 10^{17}$	
$V_{LSR}$ (km s $^{-1}$ )	7.8	5.8	
$dV/dr _{in}$ (km s $^{-1}$ pc $^{-1}$ )	0	0	(1)
$dV/dr _{out}$ (km s $^{-1}$ pc $^{-1}$ )	-0.5	2.0	(1)
$r_{br}$ (cm)	$1.75 \times 10^{17}$	$1.5 \times 10^{17}$	(1)
$\Delta V_{NT}$ (km s $^{-1}$ )	0.125	0.125	
$T_k$ (K)	10	9.5	(2)
Envelope			
$r_{max}$ (cm)	$8 \times 10^{17}$	$8 \times 10^{17}$	
$V_{LSR}$ (km s $^{-1}$ )	7.45	5.8	
$\Delta V_{NT}$ (km s $^{-1}$ )	0.625	0.500	
Molecular abundances			
$X_0(\text{NH}_3)$	$1.4 \times 10^{-8}$	$1.7 \times 10^{-8}$	(3)
$\beta$	3	1	(4)
$X_0(\text{N}_2\text{H}^+)$	$1.7 \times 10^{-10}$	$1.5 \times 10^{-10}$	(4)
$X_0(\text{C}^{18}\text{O})$	$0.5 \times 10^{-7}$	$1.5 \times 10^{-7}$	(5)
$r_{hole}(\text{C}^{18}\text{O})$ (cm)	$1.5 \times 10^{17}$	$1.75 \times 10^{17}$	(5)
$X_0(\text{CS})$	$3 \times 10^{-9}$	$3 \times 10^{-9}$	(5)
$r_{hole}(\text{CS})$ (cm)	$1.0 \times 10^{17}$	$1.15 \times 10^{17}$	(5)

- (1)  $dV/dr = dV/dr|_{in}$  if  $r < r_{br}$  and  $dV/dr = dV/dr|_{out}$  if  $r > r_{br}$
- (2) Constant for all  $r$
- (3) para- $X(\text{NH}_3) = X_0(\text{NH}_3) (n(r)/n_0)^\beta$  with  $10^{-9}$  threshold
- (4) Constant in L1517B. For L1498, abundance drops by factor 3 at  $r = 1.8 \times 10^{17}$  cm
- (5)  $X = X_0$  for  $r > r_{hole}$  and  $X = 0$  for  $r < r_{hole}$

tions for realistic core conditions. With its help, we first estimate the L1498 and L1517B temperature profiles directly from the NH<sub>3</sub> data, and then use the full Monte Carlo model to fit the observed radial profiles and spectra deriving NH<sub>3</sub> abundance profiles (and demonstrating the self consistency of the temperature determination).

To derive the temperature profiles of L1498 and L1517B, we first estimate the  $T_R^{21}$  rotation temperature for each observed position using the NH<sub>3</sub> lines. This involves fitting the hyperfine (hf) structure of the NH<sub>3</sub>(1,1) spectra (where we find that the hf components are in LTE), fitting single gaussians to the NH<sub>3</sub>(2,2) spectra, and estimating the ratio between the (2,2) and (1,1) populations (see Bachiller et al. 1987 for details). Then, we use the analytical expression derived in Appendix B to convert each rotation temperature into a gas kinetic temperature. The resulting temperature radial profiles, presented in Fig. 4, show that in each core the gas kinetic temperature is to very good approximation constant with radius and almost equal to 10 K with an rms of about 1 K.

The temperature profiles in Fig. 4 represent line-of-sight averages spatially smoothed with a 40'' gaussian (telescope resolution). To test the possibility that a realistic non-constant temperature distribution could mimic

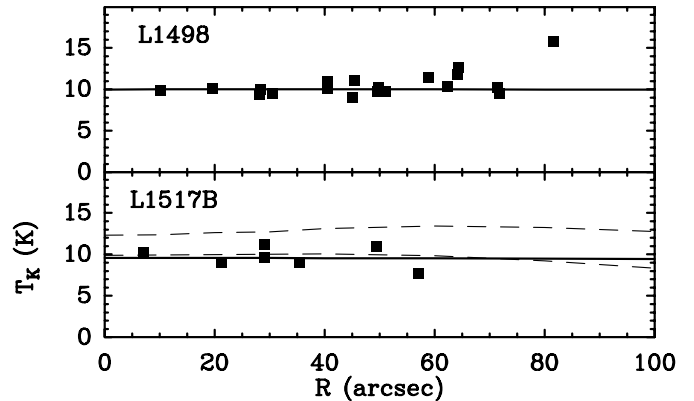


**Fig. 4.** Radial profiles of gas kinetic temperature for L1498 and L1517B derived from NH<sub>3</sub>. The squares represent real data and the solid lines represent the result of applying the same NH<sub>3</sub> analysis used for the data to spectra generated with a Monte Carlo model having constant temperature (10 K for L1498 and 9.5 K for L1517B). The dashed lines are the expected NH<sub>3</sub>-derived  $T_k$  profile for two temperature equilibrium models (see text for details).

the constant temperature profile of our NH<sub>3</sub> analysis, we have run a Monte Carlo NH<sub>3</sub> model for L1517B using the temperature law recently calculated by Galli et al. (2002) (and kindly adapted to L1517B by Daniele Galli). The synthetic NH<sub>3</sub> spectra from this model have been analyzed as the real data and used to compute an NH<sub>3</sub>-derived temperature profile. As the upper dashed line in Fig. 4 shows, a model with the “standard” cosmic ray ionization rate of  $\zeta = 3 \times 10^{-17}$  s $^{-1}$  (Goldsmith 2001), overestimates the core temperature at all radii (in fact, it overestimates the (2,2) intensity by more than a factor of 2). However, reducing  $\zeta$  by a factor of 5 (lower dashed curve) produces a temperature profile consistent with the observations (such a low  $\zeta$  value is also favored by the chemical models of the L1544 core in Taurus by Caselli et al. 2002b, but see McCall et al. 2003 for the opposite conclusion in a nearby cloud). This low  $\zeta$  temperature profile is in fact almost constant, as it has a maximum-to-minimum variation of less than 1.5 K in the region of interest. We thus conclude that the gas kinetic temperature in the L1498 and L1517B cores is constant within about 10%, and that this property is consistent a with realistic treatment of the heating and cooling of dense gas (assuming a low  $\zeta$  value).

Given the above results, we model both L1498 and L1517B as having constant temperature, and for each core, we search for the NH<sub>3</sub> abundance profile that fits simultaneously the observed (1,1) and (2,2) radial profiles of integrated intensity together with the central spectra of both transitions. We do this by using our full non LTE Monte Carlo radiative transfer analysis, and convolve the results with a 40'' gaussian to simulate an observation with the Effelsberg antenna (see Appendix B for details). For L1517B, our best model is identical to that in TMCWC, as we use the same density profile. This means that the

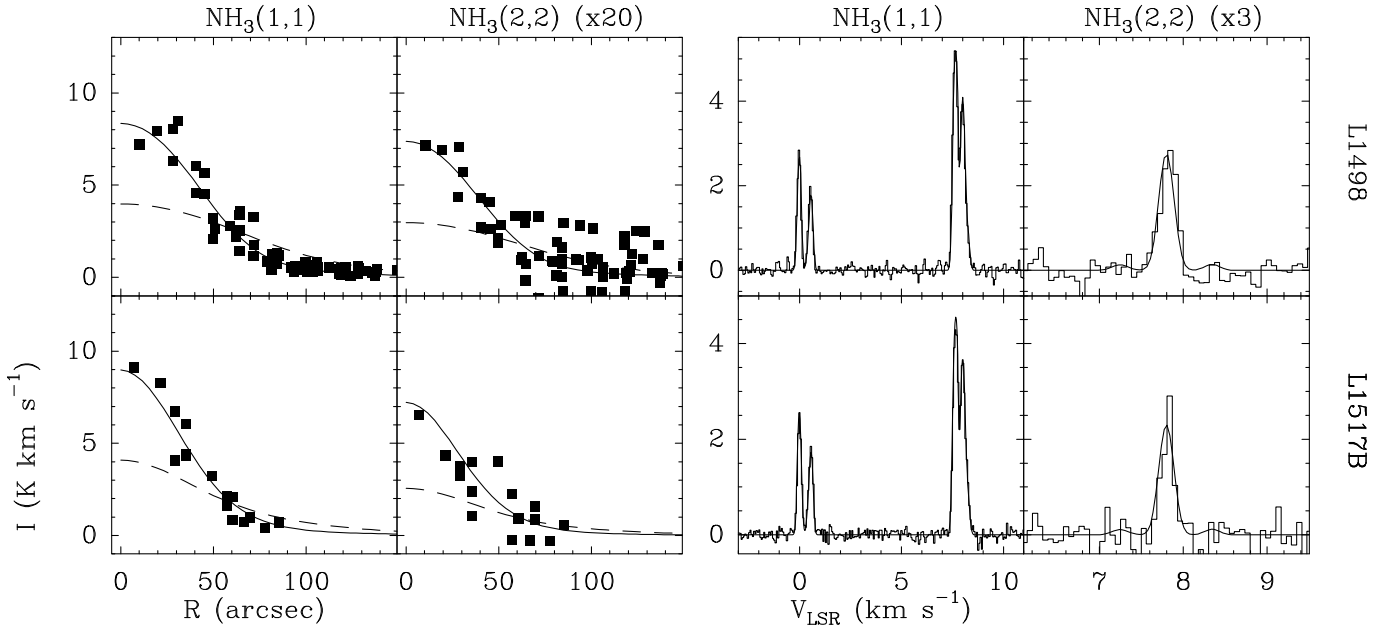


**Fig. 5.** Radial profiles of integrated intensity and central spectra of  $\text{NH}_3(1,1)$  and  $(2,2)$  towards L1498 and L1517B. The squares in the radial profiles and the histograms in the spectra represent real data. The solid lines represent the results of Monte Carlo radiative transfer models with constant temperature and a central  $\text{NH}_3$  abundance enhancement (see text). Note how they simultaneously fit the radial profiles and the central spectra (they also fit the  $\text{NH}_3$ -derived temperature profiles, see previous figure). The dashed lines in the radial profiles are models with constant  $\text{NH}_3$  abundance, chosen to fit the observations at large radius ( $\sim 60''$ ). Note how these flatter profiles cannot fit the observed central emission. The velocity scale in L1517B has been shifted by  $2 \text{ km s}^{-1}$  for presentation purposes. (Note that the 1-sigma uncertainty in the integrated intensity points is of the order of  $0.2 \text{ K km s}^{-1}$  for  $\text{NH}_3(1,1)$  and  $0.8 \text{ K km s}^{-1}$  for  $\text{NH}_3(2,2)$  multiplied by 20, and it is therefore similar to the size of the squares.)

gas temperature has a constant value of  $9.5 \text{ K}$  and that the para- $\text{NH}_3$  abundance increases inwards following the law  $X(r) = X_0(n(r)/n_0)^\beta$ , where  $X_0 = 1.7 \times 10^{-8}$  and  $\beta = 1$  (the above expression is only valid for  $X > 10^{-9}$ ). Our best fit model for L1498 is slightly different from that in TMCWC because of our improved density profile and core peak determination from the new continuum data. This model has a constant temperature of  $10 \text{ K}$  and a para- $\text{NH}_3$  abundance that increases inwards following the same law as in L1517B, but this time with  $X_0 = 1.4 \times 10^{-8}$  and  $\beta = 3$ , and again with a  $10^{-9}$  threshold. (Note that if the ortho-to-para ratio of  $\text{NH}_3$  equals 1, the total  $\text{NH}_3$  abundance is 2 times the measured para- $\text{NH}_3$  abundance.) As Fig. 5 shows, these  $\text{NH}_3$  models fit simultaneously the radial profile of integrated intensity and the central emergent spectra for both  $\text{NH}_3(1,1)$  and  $(2,2)$ . They also fit  $\text{NH}_3$ -derived temperature profiles of Fig. 4 (see solid lines).

Although initially unexpected, the higher central  $\text{NH}_3$  abundance in L1498 and L1517B is a necessary element of the radiative transfer models. To illustrate this point, we also present in Fig. 5 (dashed lines) the results of constant abundance models chosen to fit the emission at intermediate radii ( $\approx 70''$ ). As can be seen in the figure, these models predict radial profiles that are too flat for both  $\text{NH}_3(1,1)$  and  $(2,2)$ , and are therefore inconsistent with the data. The higher central abundance, thus, is unavoidable, and sets apart the  $\text{NH}_3$  molecule among all other

observed species (see Tafalla et al. 2004, in preparation, for an extensive chemical survey of L1498 and L1517B). In section 4.2 we discuss the possible origin of this behavior.

### 3.4. $\text{N}_2\text{H}^+$ : constant abundance

Like  $\text{NH}_3$ ,  $\text{N}_2\text{H}^+$  presents centrally peaked distributions in our maps of Fig. 3, and this suggests that the  $\text{N}_2\text{H}^+$  abundance does not vary greatly over the core interiors. In this section we quantify this impression by solving the  $\text{N}_2\text{H}^+$  radiative transfer with our Monte Carlo code. This code now needs to take into account the hyperfine structure introduced by the two N atoms, because (in contrast with the almost thermalized  $\text{NH}_3$ ) the  $\text{N}_2\text{H}^+$  hyperfine structure affects the line trapping and the level excitation. Unfortunately, an exact treatment of the  $\text{N}_2\text{H}^+$  radiation transfer with hf structure is not yet possible for two reasons. First, the collision rates between the individual hf components are not known, and only approximate hf-averaged values are available (see below). Second, the hf structure introduces the possibility of partial overlap between lines, complicating the problem.

TMCWC presented a simplified solution of the  $\text{N}_2\text{H}^+$  transfer which ignored the hf structure in the excitation calculation but considered it in the computation of the emergent spectrum. As mentioned there, the main problem with this approach is that it neglects the decrease

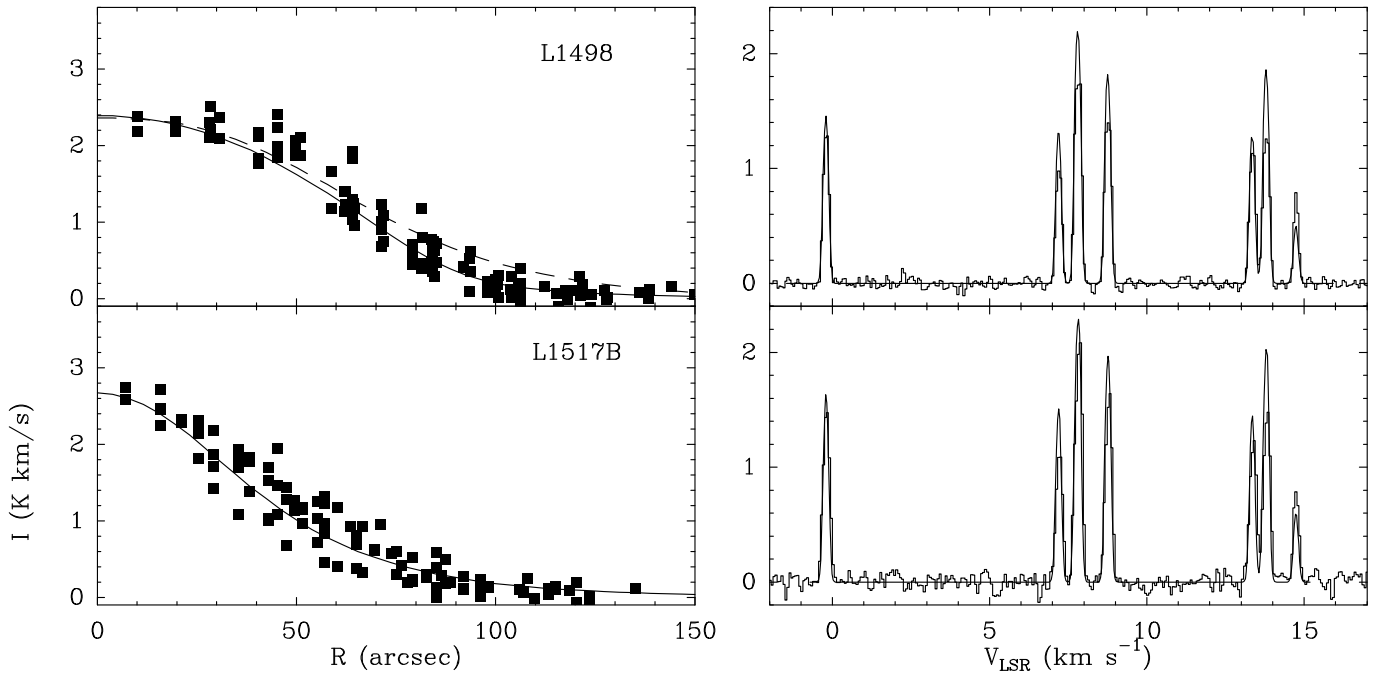


**Fig. 6.** Radial profiles of integrated emission (left) and central emerging spectra (right) for  $\text{N}_2\text{H}^+(1-0)$  toward L1498 and L1517B. Observed data are represented by squares in the radial profiles (sum of all hf components) and by histograms in the spectra (main beam brightness temperature). The solid lines represent the results from best fit Monte Carlo models: for L1517B, the model has a constant  $\text{N}_2\text{H}^+$  abundance of  $1.5 \times 10^{-10}$ , and for L1498 the model has a constant abundance of  $1.7 \times 10^{-10}$  with a drop of a factor of 3 for radii larger than  $1.8 \times 10^{17}$  cm. The dashed line in the radial profile of L1498 shows the expected emission for a constant abundance model without outer drop. The velocity scale in L1517B has been shifted by  $2 \text{ km s}^{-1}$  for presentation purposes. (Note that the 1-sigma uncertainty in the integrated intensity points is of the order of  $0.05 \text{ K km s}^{-1}$  and it is therefore smaller than the size of the squares.)

in trapping caused by the splitting. Here, to take this effect into account, we improve the model and treat explicitly the hf splitting in the low  $J$  transitions (up to  $J=2$ ), where the trapping decrease is expected to be important, while we assume the rest of transitions are degenerate (up to  $J=6$ ). This improved approach requires increasing the number of levels considered in the Monte Carlo code to 23 and the number of transitions to 44 (no line overlaps are considered). For collision rates, we use the  $\text{HCO}^+ - \text{H}_2$  rates from Flower (1999) and derive the individual coefficients between  $\text{N}_2\text{H}^+$  hf components by assuming that collisions do not distinguish between hf levels. By using these simplified collision rates and neglecting line overlaps we lose the ability to reproduce the non LTE excitation known to occur in the  $J=1-0$  line (Caselli et al. 1995). This excitation anomaly, however, seems to be a 10% effect in the level population, and therefore is of little consequence for our abundance estimate.

To better constrain the  $\text{N}_2\text{H}^+$  abundance profiles, we fit simultaneously the  $\text{N}_2\text{H}^+(1-0)$  radial profile of integrated intensity and the emergent spectra toward the core center for both  $\text{N}_2\text{H}^+(1-0)$  and  $\text{N}_2\text{H}^+(3-2)$ . We start our analysis by exploring models with constant abundance, which we find fit the data rather well. As illustrated in Fig. 6 and 7, a constant abundance model with  $X(\text{N}_2\text{H}^+) = 1.5 \times 10^{-10}$  fits automatically all L1517B observations

and no additional change is required in the abundance profile to fit this source. (Note that our model spectra are slightly brighter than the observations despite having the same integrated area because the real  $\text{N}_2\text{H}^+$  lines seem to have additional broadening, most likely caused by unresolved hyperfine structure, see section 3.7.1). For L1498, a constant abundance model with  $X(\text{N}_2\text{H}^+) = 1.7 \times 10^{-10}$  fits well both the  $J=1-0$  and  $3-2$  spectra (not shown) and almost fits the  $J=1-0$  radial profile, although it tends to overestimate the intensity at large radius (dashed lines in Fig. 6). To improve this fit, we have modified the constant abundance model by introducing an abundance drop of a factor of 3 for radii larger than  $1.8 \times 10^{17}$  cm (85'' at 140 pc). This new model fits all L1498 data rather well, as can be seen by the solid lines in Fig. 6 and 7 (the slight deviation from flat top at the center of L1498 probably arises from a similar deviation in our density profile, see Fig. 2).

In contrast with our conclusion that the  $\text{N}_2\text{H}^+$  abundance is constant or close-to-constant at the centers of L1498 and L1517B, Bergin et al. (2002) find a factor of 2 drop in the  $\text{N}_2\text{H}^+$  abundance at the center of the B68 core. Such a significant drop seems excluded in L1517B or L1498, not just from our modeling but from the lack of any significant drop in the  $\text{N}_2\text{H}^+$  emission near the continuum peak (see maps in Fig. 3). This contrast with the behavior in B68 is especially significant in the case of

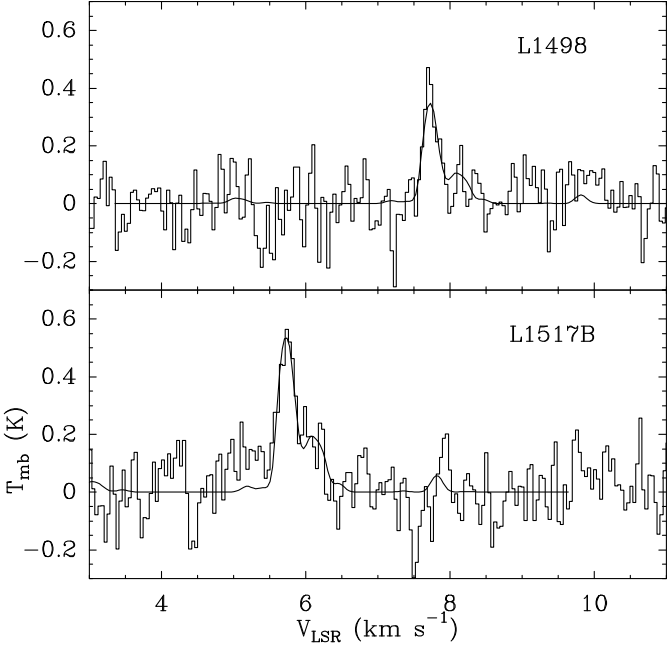


**Fig. 7.** Observed  $\text{N}_2\text{H}^+$ (3–2) spectra (histograms) and predictions (lines) for the same models shown in Figure 6. The models derived to fit the 1–0 transition also fit the 3–2 spectra. (Note that the multiple peaks in the spectra arise from hyperfine structure, and do not represent multiple velocity components.)

L1517B, as both B68 and L1517B have central densities of about  $2 \times 10^5 \text{ cm}^{-3}$  and are well fitted by isothermal models (Alves et al. 2001, our section 3.1). Given the importance of  $\text{N}_2\text{H}^+$  as a tracer of dense gas, further work should be carried out to understand the discrepancy between these cores.

### 3.5. CO isotopomers: central depletion

The central holes in the CO isotopomer maps of Fig. 3 indicate graphically that the abundance of these species drops systematically toward the peak of both L1498 and L1517B. To determine quantitatively these abundance drops, we use again the Monte Carlo radiative transfer model to fit the observations with a variable abundance profile (for further details on the Monte Carlo modeling, see TMCWC). To better constrain the abundances and to provide a self consistency check to our calculations, we use simultaneously all the CO isotopomer data we have available. Thus, in addition to fitting the  $\text{C}^{18}\text{O}$ (1–0),  $\text{C}^{18}\text{O}$ (2–1), and  $\text{C}^{17}\text{O}$ (2–1) data from the IRAM 30m telescope, we use the lower angular resolution  $\text{C}^{17}\text{O}$ (1–0) data from FCRAO already presented in TMCWC. Also, taking into account previous work on isotopic abundances in the ISM, we assume a constant  $\text{C}^{18}\text{O}/\text{C}^{17}\text{O}$  abundance ratio of 3.65 (Penzias 1981). In this way, our determination of the CO isotopomer abundances reduces for each core to finding a single abundance profile that fits simultaneously four

radial profiles of integrated intensity and four emergent spectra.

Before attempting to reproduce the observations, we test the conclusion that constant abundance models cannot fit the data from neither L1498 nor L1517B. To do this, we fix the  $\text{C}^{18}\text{O}$  abundance so that the models fit the observations at a radius of  $100''$ , and compare the model predictions with the observations at smaller radii. As the dashed lines in the radial profiles of Fig. 8 show, the constant abundance models fail to fit the data for all CO isotopomers in both L1498 and L1517B. They do so by a wide margin (more than a factor of 2), and this proves that constant abundance  $\text{C}^{18}\text{O}/\text{C}^{17}\text{O}$  models are inconsistent with observations. A sharp drop of abundance toward the center is therefore required.

To model the CO central abundance drop, we have explored different abundance profiles, starting with the exponential forms introduced by TMCWC ( $X \sim \exp(-n(r))$ ). Our higher angular resolution data, however, suggest that these forms do not provide a fast enough abundance drop to fit the integrated intensity near the core centers, and that faster decreases are needed to reproduce the data (note that because of the central flattening of the density profiles, the exponential forms do not necessarily result in dramatic abundance drops). Thus, we have explored alternative abundance profiles, like squares of the exponential forms or central holes. Unfortunately, if the abundance toward the core center is low enough that the emission is dominated by the outer layers (order of magnitude drop), the exact form of the abundance profile is not very critical. Given this degeneracy of the solution, we have chosen the simplest form, a (step) central hole, and used it as basic model for the CO (and CS) abundance profiles in L1498 and L1517B. Although in some cases a slightly different abundance profile may produce a better fit to the integrated intensity radial profile (as in the case of CS in L1517B, see below), we have preferred for consistency and inter-comparability to fit all the abundance drops with central holes.

Fig 8 shows a comparison between the central hole models (solid lines) and the observations for both L1498 and L1517B. These models are characterized by just two parameters (external abundance and hole radius, see Table 3) and provide a simultaneous fit to the four integrated intensity radial profiles and the four central spectra of  $\text{C}^{18}\text{O}$  and  $\text{C}^{17}\text{O}$ . Their ability to fit the data shows that the central abundance drop in each core is sudden and deep, and that the data are consistent with both L1498 and L1517B having no CO molecules in their innermost region ( $r < 70''$ ). Although the radius of the central hole is not uniquely determined by the observations (it is slightly coupled to the initial abundance estimate), the true values cannot be very far from our estimates. Thus, we combine the radius of the abundance drop (Table 3) with the density profiles (Table 2) in order to estimate that the density at which CO molecules disappear from the gas phase is  $7.8 \times 10^4 \text{ cm}^{-3}$  for L1498 and  $2.5 \times 10^4 \text{ cm}^{-3}$  for L1517B.

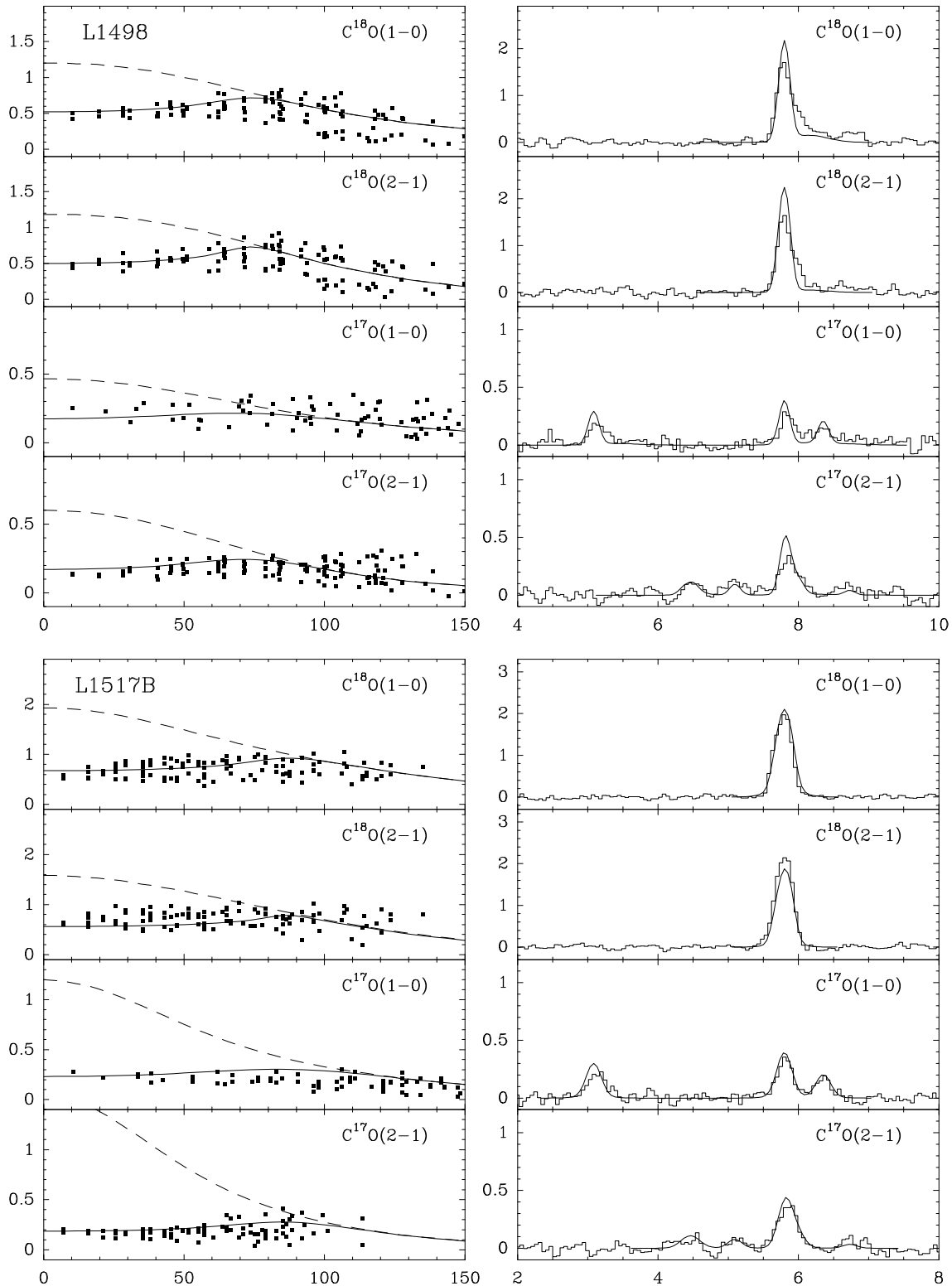


**Fig. 8.** Radial profiles of integrated emission (left) and central emerging spectra (right) for  $\text{C}^{18}\text{O}(1-0)$ ,  $\text{C}^{18}\text{O}(2-1)$ ,  $\text{C}^{17}\text{O}(1-0)$ , and  $\text{C}^{17}\text{O}(2-1)$  toward L1498 and L1517B. Observed data are represented by squares in the radial profiles and by histograms in the spectra (main beam brightness temperature). The dashed lines represent constant abundance models chosen to fit the emission at radius  $100''$  ( $\text{X}(\text{C}^{18}\text{O}) = 0.5 \times 10^{-7}$  in L1498 and  $1.5 \times 10^{-7}$  in L1517B) and, as the figure shows, they fail to fit the central emission by a large margin. The solid lines are models with the same abundance value for large radii but having a central hole with no molecules ( $r_{\text{hole}} = 71''$  for L1498 and  $83''$  for L1517B). These models fit simultaneously all transitions at all radii. A  $\text{C}^{18}\text{O}/\text{C}^{17}\text{O}$  isotopic ratio of 3.65 is assumed in both cores. (Note that the 1-sigma uncertainty in the integrated intensity points is of the order of  $0.03 \text{ K km s}^{-1}$  and it is therefore similar to the size of the squares.)

### 3.5.1. Deviations from spherical symmetry

Our radiative transfer analysis has assumed spherical symmetry, and our Monte Carlo models have been used to fit azimuthal averages of the observed emission. This means that our radial profiles with a central abundance drop represent spherical averages of the distribution of CO molecules in each core. As the maps in Fig. 3 show, however, the distribution of CO emission in both L1517B and L1498 is not fully circular (or elliptical), and superposed upon the central emission drop, there is a pattern of secondary peaks and valleys. In L1517B, for example, the CO emission is brighter toward the west, and in L1498 there are bright spots toward the southeast and the west. The asymmetries in the CO emission appear in all transitions but do not have counterparts in the continuum or  $\text{NH}_3$  emission (Fig. 3). This suggests that they do not arise from asymmetries in the distribution of density or temperature, but that they result from true non-azimuthal asymmetries in the distribution of CO abundance. The detailed modeling of these asymmetries is outside the scope of our spherically symmetric radiative transfer analysis, but a simple inspection of the maps in Fig. 3 suggests that the abundance variations needed to produce them are at the level of a factor of two. These variations, therefore, are only perturbations on the (order of magnitude) drop in abundance at high densities, but as we will see in section 4.3, they offer interesting clues concerning the process of core formation.

### 3.6. CS: central depletion

We finish our abundance analysis studying the distribution of the CS molecule. Unfortunately, its emission is more difficult to model because the CS lines from both cores are very optically thick and strongly self absorbed. This can be seen in Fig. 9, where the main CS isotopomer lines appear asymmetric and double-peaked while the spectra of the rare  $\text{C}^{34}\text{S}$  species are single gaussians. These self absorbed spectra depend strongly on the physical parameters of the low-excitation outermost layers that give rise to the absorption ( $r > 0.1$  pc) and for which we have very little information in terms of density and temperature. Thus, although the Monte Carlo code can treat accurately the transfer of radiation under optically thick conditions, our CS modeling is limited by our ignorance of the gas properties in the outer core regions. If these properties deviate from the extrapolation of our simple models, the radiative transfer solution for the main isotopomer of CS is compromised. To minimize this effect, we have complemented our CS observations with  $\text{C}^{34}\text{S}$  data.

As with CO, we test the CS models simultaneously against our full CS isotopomer data set, which consists of maps and spectra of CS(2-1) and CS(3-2), and central spectra of  $\text{C}^{34}\text{S}(2-1)$  and  $\text{C}^{34}\text{S}(3-2)$  (plus a full  $\text{C}^{34}\text{S}(2-1)$  map of L1498). To minimize the number of free parameters, we set the CS/ $\text{C}^{34}\text{S}$  isotopic ratio to its solar value of 22.7, since this number seems consistent with ISM de-

terminations (Lucas & Liszt 1998). An acceptable abundance curve, therefore, must fit simultaneously the 4 emergent spectra and 2 radial profiles (3 in L1498) shown in Figure 9.

Our first set of Monte Carlo models have spatially constant CS abundance, set to a value that fits the integrated intensity radial profile at a radius of 100''. As the dashed lines in Fig. 9 show, these constant abundance models predict a significant concentration of the emission toward the core center, which is not seen in the data. This is more evident in L1517B because of its higher central density concentration, but is also clear in the flatter and more CS-opaque L1498 core, especially in the thinner  $\text{C}^{34}\text{S}(2-1)$  line, where the central deviation between model and data is of at least a factor of two. The failure of the constant abundance models to fit the data proves that the CS abundance must drop toward the centers of both L1498 or L1517B (in agreement with previous lower resolution results, see Kuiper et al. 1996 and TMCWC).

To model the central decrease of the CS abundance, we have again explored different families of abundance profiles. Models with a central hole, for example, seem slightly superior to exponential drop models in the case of L1498, although both models fit the data in L1517B. Unfortunately, a detailed comparison between the different forms of the central abundance drop is difficult because of the dependence of the results on the CS self absorption, and for this reason, we only present the results of models with a central hole. These models provide reasonable fits to the observations, as illustrated in Fig. 9, which shows that central hole models (solid lines) match simultaneously for each core all radial profiles of integrated intensity and all central spectra.

The simultaneous fit of both the self absorbed CS lines and the gaussian  $\text{C}^{34}\text{S}$  spectra is a critical test for the models. The CS self absorption arises as a natural consequence of the combination of high optical depth and subthermal excitation in the model low-density outer layers, and this makes this feature the most sensitive tracer of the velocity field in the outer core (as mentioned in section 3.2). The red shifted CS selfabsorption in L1498 indicates a contraction motion, while the blue shifted self absorption in L1517B requires expansion (in agreement with previous work, see Kuiper et al. 1996; Lee et al. 1999, and TMCWC). These velocity gradients, however, do not continue all the way to the core center, since otherwise the central  $\text{C}^{34}\text{S}$  spectra would not have the same linewidth (within the noise) as the  $\text{N}_2\text{H}^+$  and  $\text{NH}_3$  lines. Thus, we have parametrized the velocity field as constant up to a radius of  $1.75 \times 10^{17}$  cm (83'') in L1498 and  $1.5 \times 10^{17}$  cm (71'') in L1517B, and then as increasing/decreasing linearly with radius for larger distances (Table 3). To fit the broader CS(2-1) self absorption and the slight wing in L1498, we have additionally required that the CS abundance increases by a factor of 5 in the outer envelope ( $r > 4 \times 10^{17}$  cm  $\approx 190''$ ). As mentioned in section 3.2, however, this envelope most likely represents a foreground red component that also gives rise to a red

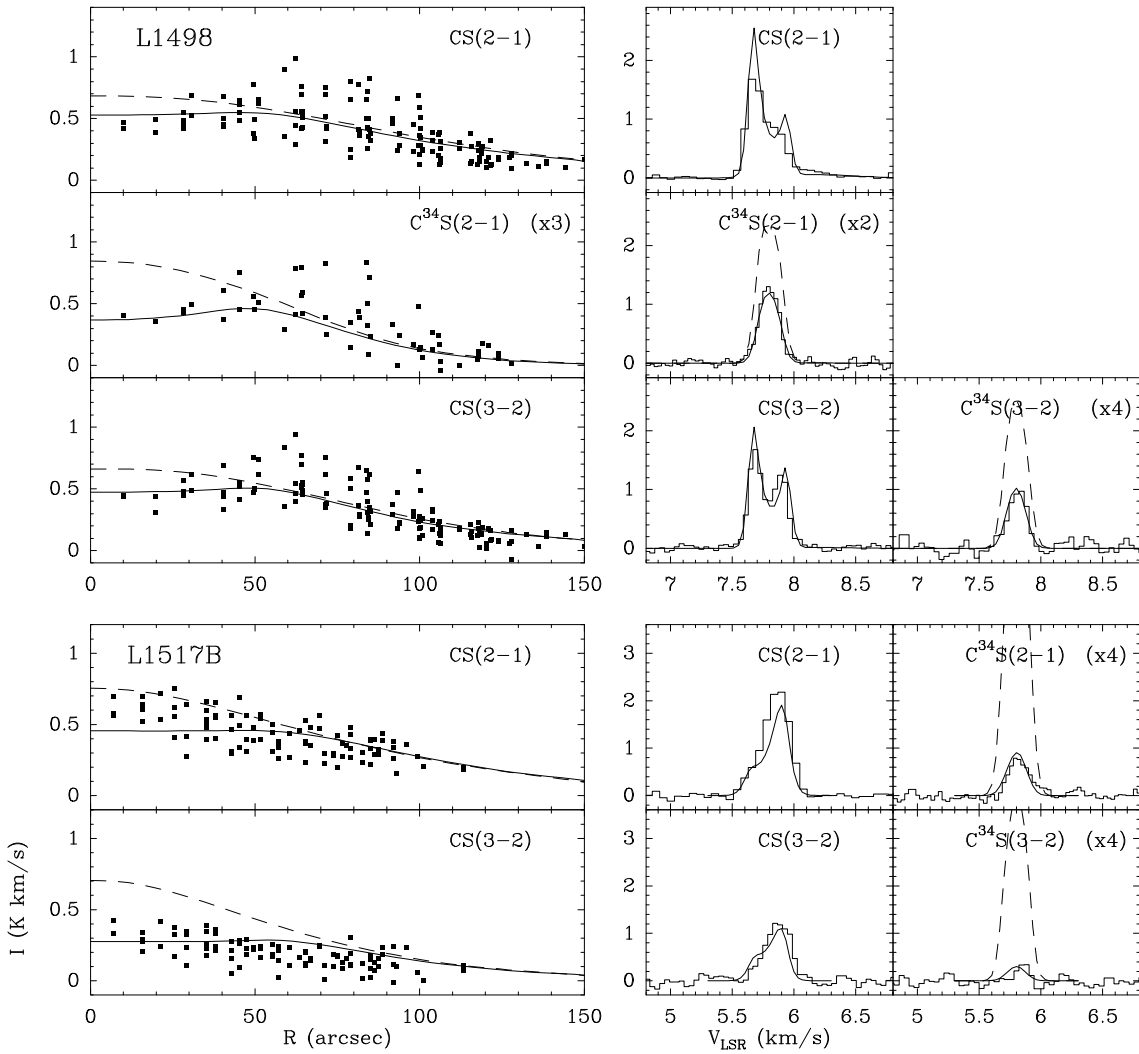


**Fig. 9.** Radial profiles of integrated emission (left) and central emerging spectrum (right) for CS(2-1), CS(3-2),  $\text{C}^{34}\text{S}(2-1)$ , and  $\text{C}^{34}\text{S}(3-2)$  toward L1498 and L1517B. Observational data are represented by squares in the radial profiles and by histograms in the spectra (main beam brightness temperature). The dashed lines represent constant abundance models chosen to fit the emission at radius  $100''$  ( $\text{X}(\text{CS}) = 3 \times 10^{-9}$  in both L1498 and L1517B) and, as the figure shows, they fail to fit the central emission by a large margin. The solid lines are models with the same abundance value for large radii but having a central hole with no molecules ( $r_{\text{hole}} = 48''$  for L1498 and  $55''$  for L1517B). These models fit simultaneously all transitions at all radii. A CS/ $\text{C}^{34}\text{S}$  isotopic ratio of 22.7 is assumed in both cores. (Note that the 1-sigma uncertainty in the integrated intensity points is of the order of  $0.03 \text{ K km s}^{-1}$  and it is therefore similar to the size of the squares.)

wing in the  $\text{C}^{18}\text{O}$  spectra (Fig. 8, see also Lemme et al. 1995). Foreground contamination, in fact, may also be the cause of the blue shifted self absorption in L1517B, as the nearby L1517A core is slightly blue shifted with respect to L1517B (Benson & Myers 1989). Thus, the velocity gradients traced with the CS self absorption most likely reflect the conditions in the region where the cores meet the extended ambient cloud ( $r > 0.1 \text{ pc}$ ) and not an intrinsic core velocity pattern. Although these motions affect strongly the shape of the CS spectra, they seem to involve only the core outermost layers and not the dense (probably star-forming) part. Their interpretation as global core contraction or expansion patterns seems therefore not warranted.

The reasonable fit provided by the central-hole models shows that the CS abundance drop in L1498 and L1517B is as dramatic as that of CO. This implies that the centers of these two cores may lack CS molecules for radii smaller than  $48''$  in L1498 and  $55''$  in L1517B (Table 3), and that the CS emission in these systems only traces the outer core layers. As with CO, we can convert the radius of the central hole into a critical density above which CS molecules disappear from the gas phase. Using the density profiles of Section 3.1, we derive a maximum density of  $8 \times 10^4 \text{ cm}^{-3}$  for L1498 and  $4 \times 10^4 \text{ cm}^{-3}$  in L1517B, which are similar to but slightly larger than those measured for the CO isotopomers. Thus, CS seems to freeze-out from the gas phase at slightly larger densities than CO, and

therefore traces slightly more central parts of cores. The innermost core regions, however, are totally invisible in CS, even when observed with optically thin C<sup>34</sup>S emission.

A look at the maps of Fig. 3 shows that the CS emission presents the same azimuthal asymmetries found in CO: relative maxima toward the SE and W in L1498 and toward the W in L1517B. This similarity with the pattern of C<sup>18</sup>O asymmetries and the fact that in L1498 the asymmetry can also be seen in the thinner C<sup>34</sup>S(2–1) emission strongly suggest that these features are real and not the result of self absorption effects. Thus, following the arguments presented in the study of CO (section 3.5.1), we conclude that in each core the distribution of CS abundance is not azimuthally symmetric. As in CO, this azimuthal asymmetry probably arises from changes in the abundance of a factor of a few and is superposed upon the order-of-magnitude central abundance drop. A full discussion of its possible origin in terms of core formation history is deferred to section 4.3.

### 3.7. Gas kinematics

Our modeling of the line profiles toward the center of L1498 and L1517B has sampled the gas velocity field along the central line of sight of each core. This field has been found to have a turbulent component approximately constant with radius, with a possible increase in the outer part of L1498 (but most likely due to another velocity component). The line-of-sight systemic velocity seems also constant over the center of the cores, although it presents gradients in the outer layers: contraction in L1498 and expansion in L1517B. In this section, we turn our attention to the 2-dimensional (plane of the sky) velocity field as a complement to the analysis of the central line-of-sight. To do this, we make gaussian fits to the spectra at all positions and we study the spatial variations of the fit results. As only N<sub>2</sub>H<sup>+</sup> and NH<sub>3</sub> are sensitive to the core dense gas, we only use these species in our velocity study. Both N<sub>2</sub>H<sup>+</sup> and NH<sub>3</sub> have the additional advantage of having hyperfine structure, which allows for correction of optical depth effects in the linewidth determination.

#### 3.7.1. Gas turbulence

We study the spatial distribution of the gas turbulent component using the intrinsic linewidths derived from the hf fits and determining their radial profiles as we have done before with the integrated line intensities. As the intrinsic linewidth is the sum in quadrature of a thermal and a non thermal component (e.g., Myers 1983), and the thermal part is constant because the gas kinetic temperature is constant (section 3.3), any spatial variation of the intrinsic linewidth has to result from an equivalent spatial variation of the non-thermal (turbulent) part.

Fig. 10 presents the radial profiles of the NH<sub>3</sub>(1,1) and N<sub>2</sub>H<sup>+</sup>(1–0) intrinsic linewidths  $\Delta V$  for both L1498 and L1517B. A simple inspection of these profiles suggests

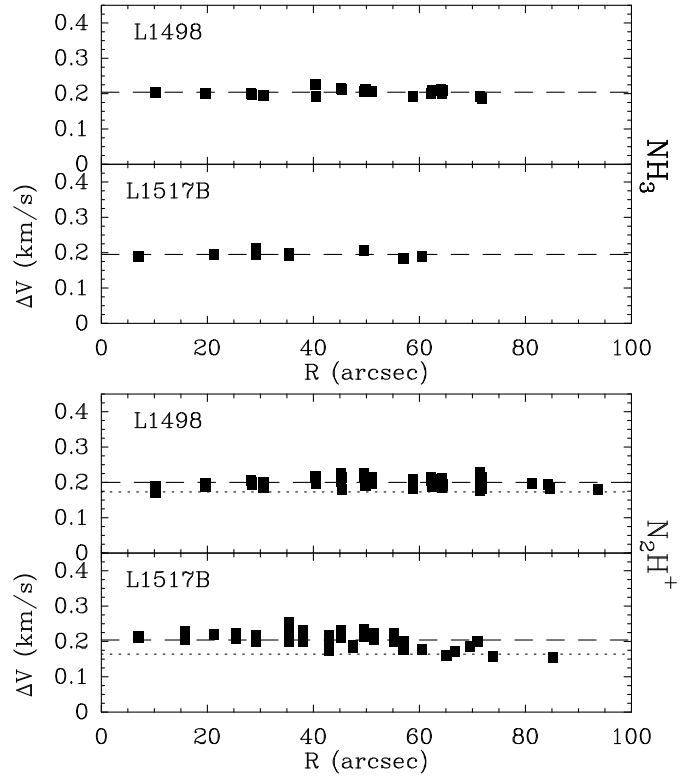


**Fig. 10.** Radial profiles of intrinsic linewidth for L1498 and L1517B from NH<sub>3</sub> and N<sub>2</sub>H<sup>+</sup> hyperfine-structure fits. Note the lack of systematic variations and the extremely low dispersion. The long-dashed horizontal lines indicate the average value for each core and molecule (very close to 0.20 km s<sup>-1</sup> in all cases). The short-dashed lines indicate the N<sub>2</sub>H<sup>+</sup> linewidth expected when adding the nonthermal component derived from NH<sub>3</sub> to a thermal N<sub>2</sub>H<sup>+</sup> component at 10 K (see text for details). To maximize sensitivity, only points with integrated intensity larger than 1.3, 1, 0.6, and 0.6 K km s<sup>-1</sup> are presented for L1498 NH<sub>3</sub>, L1517B NH<sub>3</sub>, L1498 N<sub>2</sub>H<sup>+</sup>, and L1517B N<sub>2</sub>H<sup>+</sup>, respectively. (As indicated in the text, the 1-sigma uncertainty of the linewidth estimates, both from NH<sub>3</sub> and N<sub>2</sub>H<sup>+</sup>, is of the order of 0.01 km s<sup>-1</sup>, and it is therefore smaller than the size of the squares.)

that there is no significant trend of increase or decrease of linewidth as a function of radius, meaning that any non thermal component is also spatially constant over both cores. To test for the presence of a hidden slope in the linewidth distribution, we have fitted the points in Fig. 10 with a function of the form  $\Delta V = a + bR$ , where  $R$  is the radius in arcseconds and  $a$  and  $b$  are two free parameters. In three out of four cases the  $b$  coefficient is smaller than its *rms*, hence the fit is consistent with  $b = 0$  and the distribution of  $\Delta V$  is independent of radius. In the fourth case (L1517B N<sub>2</sub>H<sup>+</sup> data), the slope is negative, and the linewidth slightly decreases with radius (only by 30% in 100''). This slight decrease, which can be seen in the data at large radii, is most likely due to errors in the N<sub>2</sub>H<sup>+</sup> hfs fit (see below) and has no counterpart in the

$\text{NH}_3$  linewidth distribution. We therefore conclude that the non thermal component of the velocity field in both L1498 and L1517B is constant with radius for as far as we can measure.

The finding of constant linewidth in L1498 and L1517B agrees with the results of Barranco & Goodman (1998), who found the same behavior in the interior of four other dense cores. These authors, however, suggested that linewidths may increase at the largest observed radii, a behavior not seen in our data. Even if we include the low sensitivity points at very large radii, the constant linewidth trend of Fig. 10 remains unchanged, and the scatter due to noise dominates the plots. We therefore conclude that the linewidth does not increase with radius, or if it does, it starts increasing at a larger radius than suggested by Barranco & Goodman (1998).

A puzzling result from our hf analysis is that the  $\text{N}_2\text{H}^+(1-0)$  and  $\text{NH}_3(1,1)$  linewidths are almost equal (very close to  $0.20 \text{ km s}^{-1}$ ). This is unexpected because the  $\text{N}_2\text{H}^+$  molecule is 1.7 times heavier than  $\text{NH}_3$  and thus its thermal component is 1.3 times smaller. If both molecules are tracing the same gas, their turbulent components should be equal, and the lighter  $\text{NH}_3$  should always present broader lines. To quantify this problem, we have assumed that the  $\text{NH}_3$  hf fit returns the true linewidth (thermal plus turbulent), and we have derived its non-thermal part by subtracting a thermal component at 10 K. When this nonthermal component is added to the  $\text{N}_2\text{H}^+$  thermal part, we find that the  $\text{N}_2\text{H}^+$  linewidths derived from the hf fit are approximately 20% larger than expected, as illustrated in Fig. 10, where the dotted line is the expected  $\text{N}_2\text{H}^+$  linewidth.

The origin of the larger  $\text{N}_2\text{H}^+$  non-thermal component is unclear. Different linewidths for ions and neutrals are expected in the presence of magnetic fields, but the observed trend in both L1498 and L1517B (larger non-thermal component in the ion line) is opposite to what is expected theoretically (Houde et al. 2000). A more likely explanation is that the  $\text{N}_2\text{H}^+$  hf fit overestimates the linewidth by about 20%. This is so because the hf analysis of both molecules assumes LTE among hf components, but this is only correct for the  $\text{NH}_3$  lines.  $\text{N}_2\text{H}^+$  is notorious for showing non-LTE excitation among its components (Caselli et al. 1995), and this violates a main assumption of the analysis. In addition, as our data show and was first noticed by Caselli et al. (1995), there is a discrepancy between the  $\text{N}_2\text{H}^+$  linewidth derived from the hf fit and the linewidth measured by a Gaussian fit to the thinnest (reddest) component. This component appears slightly (5-10 %) narrower than the hf-fit linewidth, contrary to what would be expected if the hf fit truly corrected for optical depth broadening. This suggests that  $\text{N}_2\text{H}^+$  linewidths derived from standard hf fits may be slightly overestimated (20%), either because of a failure in the LTE analysis or because of the presence of additional hyperfine splitting due to magnetic spin-rotation interaction of the H atom (the latter option seems less likely according to recent estimates of the splitting, Luca Dore private communication).

Of course, this suggestion does not contradict our conclusion that the linewidth is constant in L1498 and L1517B, as it is confirmed independently (with even less scatter) by the more reliable  $\text{NH}_3$  analysis (Fig. 10). According to this analysis, the mean intrinsic ( $\text{NH}_3$ ) linewidth is  $0.204 \text{ km s}^{-1}$  in L1498 and  $0.196 \text{ km s}^{-1}$  in L1517. Subtracting thermal components of 10 K for L1498 and 9.5 K for L1517B (section 3.3), we estimate non thermal turbulent (FWHM) linewidths of  $0.121 \text{ km s}^{-1}$  in L1498 and  $0.113 \text{ km s}^{-1}$  in L1517B (note that our Monte Carlo models use  $0.125 \text{ km s}^{-1}$  as a compromise to fit both  $\text{NH}_3$  and the broader  $\text{N}_2\text{H}^+$ ).

Even if the turbulent linewidth is constant with radius on average, it may still present random variations across each core, and to explore this possibility we compare the measured  $rms(\Delta V)$  of  $\text{N}_2\text{H}^+$  and  $\text{NH}_3$  ( $\approx 10^{-2} \text{ km s}^{-1}$ ) with the value expected from the noise level in the data. To calculate this expected  $rms$ , we have created at each L1498 and L1517B position a pair of simulated  $\text{N}_2\text{H}^+$  and  $\text{NH}_3$  spectra with the correct intensity and noise level, but with all positions having the same linewidth. These simulated data result from averaging all spectra of each molecule and core, creating a high S/N spectrum which has then been scaled for each position to match the observed integrated intensity, with noise added to match the observed noise level (the averaging process broadens the line due to velocity fields, but by less than 10%). This artificial data set has then been subject to the same hf analysis as the real data, so its  $rms(\Delta V)$  provides a direct measure of the effect of noise on the measured linewidth. Comparing this  $rms(\Delta V)$  with that measured from the real data, we find that  $rms(\Delta V)$  of the real data is  $1.1 \pm 0.3$ , times the  $rms(\Delta V)$  of the simulated data, which means that the observed dispersion is consistent with noise, and that there is no evidence for an additional source of linewidth variations. This result, which agrees with the line-of-sight analysis of the Monte Carlo modeling, indicates that the data are consistent with a single  $\Delta V$  value in the inner core ( $r < 0.05 \text{ pc}$ ) within better than  $0.01 \text{ km s}^{-1}$  (5%).

### 3.7.2. Velocity gradients

The other kinematic parameter derived from the hf fit of the  $\text{NH}_3$  and  $\text{N}_2\text{H}^+$  spectra is the line center velocity. As with the linewidth, we have made radial profiles of the line center velocity for both  $\text{NH}_3$  and  $\text{N}_2\text{H}^+$  in L1498 and L1517B, and they are presented in Fig. 11. These radial profiles are flat on average, and their scatter around the mean is larger than the scatter in linewidth by a about a factor of 2. This larger scatter of the line center velocity is significant according to the model of simulated spectra used in the previous section, because the hf analysis is more sensitive to the line center velocity than to the linewidth, especially for  $\text{N}_2\text{H}^+$ . Comparing the data with the model, we estimate that the observed scatter in the line center velocity is  $0.03 \text{ km s}^{-1}$ , or  $5.4 \pm 2.5$  times larger

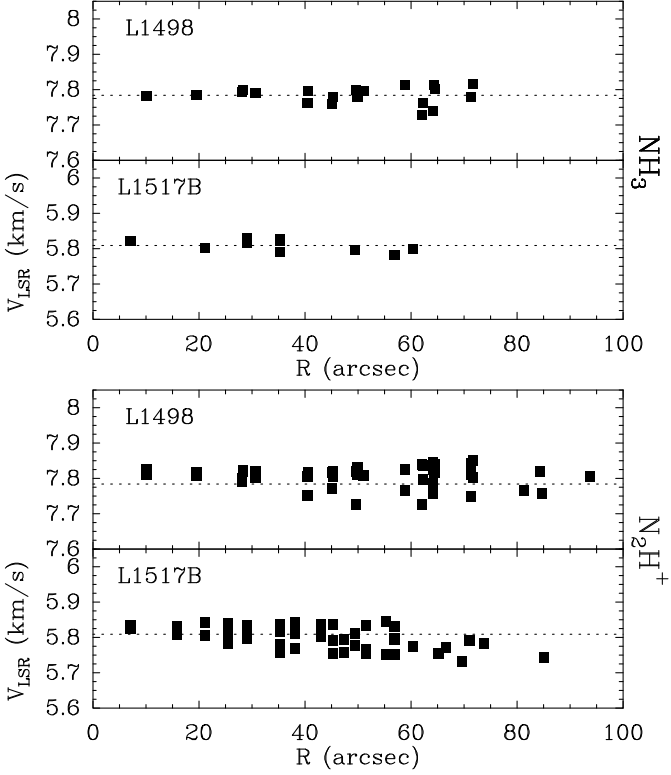


**Fig. 11.** Radial profiles of line center velocity for L1498 and L1517B derived from  $\text{NH}_3$  and  $\text{N}_2\text{H}^+$  hyperfine-structure fits. The dispersion of the points indicates the presence of bulk internal motions. Intensity threshold as in Fig. 10. (As indicated in the text, the 1-sigma uncertainty of the velocity estimates, both from  $\text{NH}_3$  and  $\text{N}_2\text{H}^+$ , is of the order of  $0.005 \text{ km s}^{-1}$ , and it is therefore smaller than the size of the squares.)

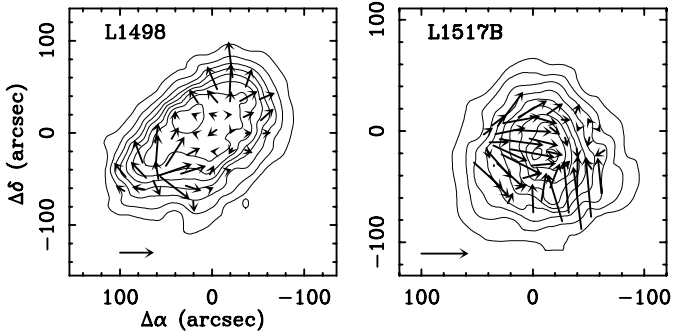


**Fig. 12.** Gradients of  $V_{\text{LSR}}$  from  $\text{N}_2\text{H}^+$  hf fits. The arrows indicate both the direction (from low to high  $V_{\text{LSR}}$ ) and intensity of the gradient (the arrows in the bottom left corners represent gradients of  $3 \text{ km s}^{-1} \text{ pc}^{-1}$ ). The contours are  $\text{N}_2\text{H}^+$  integrated intensity maps.

than it should be if all positions had exactly the same velocity. This implies that the  $V_{\text{LSR}}$  variations seen in the radial profiles of Fig. 11 correspond to real changes in the gas velocity across the core and not just to noise.

To study the origin of the velocity changes, we first determine their spatial distribution. Using a program sim-

ilar to that of Caselli et al. (2002a), we have calculated at each map position the local velocity gradient, both in modulus and direction, by comparing the  $V_{\text{LSR}}$  velocity of each point with that of its neighbors. A graphical representation of the  $\text{N}_2\text{H}^+$  results is shown in Fig. 12, and similar plots, but with fewer points, were derived for  $\text{NH}_3$  (their similarity confirms that the velocity fluctuations represent real velocity variations). As these maps show, both the direction and modulus of the velocity gradient change across both L1498 and L1517B, indicating that the gradients do not originate from simple global velocity patterns like rotation. This lack of global patterns, however, does not imply that the velocity variations are completely random, because the gradients are correlated over areas larger than the telescope beam ( $26''$ ) or the area used to measure individual velocity gradients ( $40''$ ). They therefore have to arise from bulk gas motions that affect sizeable fractions of the core material.

As a first estimate of the importance of these motions, we calculate the average velocity gradient for each core. Both  $\text{N}_2\text{H}^+$  and  $\text{NH}_3$  give consistent results, especially for the position angle (-20 and -75 degrees for L1498 and L1517B, respectively). For the modulus of the gradient, the  $\text{NH}_3$  data give a slightly lower value (10% for L1498 and 40% for L1517B), so we average the  $\text{N}_2\text{H}^+$  and  $\text{NH}_3$  values and derive  $0.75$  and  $1.1 \text{ km s}^{-1} \text{ pc}^{-1}$  for L1498 and L1517B, respectively. These values are similar to those found by Goodman et al. (1993) in other cores, again an indication that L1498 and L1517B are representative Taurus cores. Our value for L1498, in addition, is in excellent agreement with a similar estimate by Caselli et al. (2002a). The gradients measured in this manner, however, are strict lower limits, as in addition to the average across the sky required to estimate the mean gradient, the velocity estimate at each position already represents an average along the line of sight. This average necessarily cancels spatial variations of the velocity, given the lack of coherence over scales of a core diameter (Fig. 12). Unfortunately, this effect cannot be corrected without a full model of the core kinematics, and as a simple alternative for estimating the velocity differences between parts of the core, we measure the spread of  $V_{\text{LSR}}$  in Fig. 11, which is approximately  $0.1 \text{ km s}^{-1}$  ( $= 3 \times \text{rms}$ ). The noise contribution to this spread is negligible according to our synthetic spectra model ( $3 \times \text{rms} = 0.013 \text{ km s}^{-1}$ ), so we can consider that the scatter represents true velocity variations. It is possible that part of this dispersion arises from a global component (e.g., rotation), but the results in Fig. 12 show that this component cannot be dominant. Crudely assuming equipartition, we estimate the internal core motions to be at least  $0.05 \text{ km s}^{-1}$ , although they can be as high as  $0.1 \text{ km s}^{-1}$ .

Although the gas motions are small and subsonic (sound speed is  $0.19 \text{ km s}^{-1}$  for  $10 \text{ K}$ ), and therefore have little effect on the core energy budget, their presence indicates that the cores have not yet attained a state of perfect hydrostatic equilibrium. How these motions originate is unclear, but several indications suggest that they

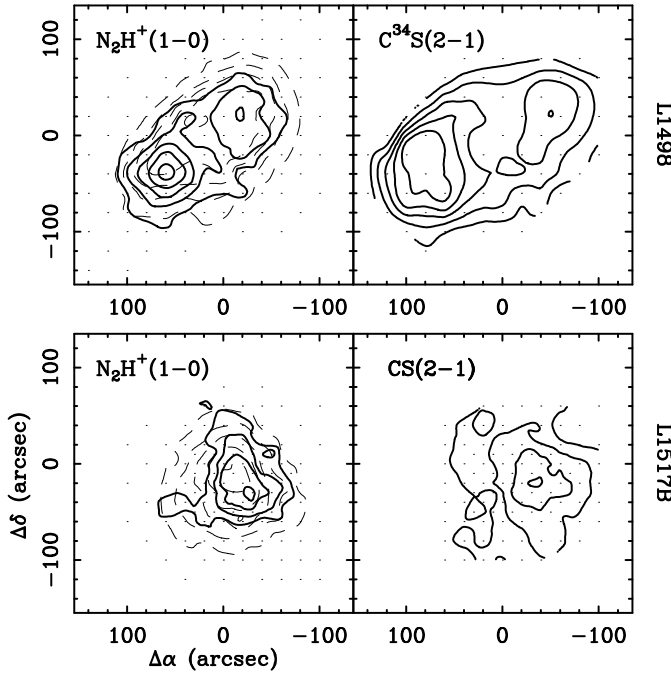


**Fig. 13.** Comparison of “high velocity”  $\text{N}_2\text{H}^+$  emission to  $\text{C}^{34}\text{S}$  or CS emission showing their similar distribution. This is an indication that the gas velocity structure is related to the deviations from spherical symmetry in the pattern of molecular freeze out, probably due to asymmetries in the core contraction history (see text). The solid lines in the left panels are  $\text{N}_2\text{H}^+$  integrated intensity maps for velocity intervals  $0.2 \text{ km s}^{-1}$  (one linewidth, see Fig. 10) away from the line center velocity (towards blue for L1517B and towards red for L1498) and  $0.2 \text{ km s}^{-1}$  wide. The  $\text{C}^{34}\text{S}$  or CS maps in the right panels and the full integrated  $\text{N}_2\text{H}^+$  map (dashed) are as in Fig. 3.

are related to the process of core formation. First, the motions are similar in magnitude to the inward motions observed in other cores (Lee et al. 1999, 2001), and these are believed to be associated with core contraction (note that L1498 has also infall asymmetry, while L1517B has the opposite). Second, the time scale of these motions is of the order of 1 Myr ( $0.05 \text{ km s}^{-1}$  over  $0.05 \text{ pc}$  or  $75''$ ), a typical starless core lifetime (Lee & Myers 1999). Finally, and more important, there is a correlation between some velocity components and the non azimuthal asymmetries in the abundance of the depleted molecules (CS and CO). These abundance asymmetries are most likely related to different contraction times of different parts of the core (section 4.3), and thus their correlation with the velocity pattern suggests that the pattern is related to contraction. To show this, we present in Figure 13 (left panels) the distribution of “high velocity”  $\text{N}_2\text{H}^+$  emission (blue for L1498 and red for L1517B) superposed upon the integrated  $\text{N}_2\text{H}^+$  emission (see caption for details). As the right panels in the figure show, these “high velocity”  $\text{N}_2\text{H}^+$  components have distributions remarkably close to the distribution of bright CS/ $\text{C}^{34}\text{S}$  spots (more so than to CO probably because CS and  $\text{N}_2\text{H}^+$  are sensitive to similar

densities), which we have seen most likely arise from differences in the amount of CS freeze-out. The similar distributions are more remarkable because CS and CO hardly coexist with  $\text{N}_2\text{H}^+$ , as they deplete at radii for which  $\text{N}_2\text{H}^+$  is non-detectable, and suggest a correlation of high CS abundance with the “high velocity” components. As we will see below, these high CS-abundance spots most likely arise from material that has been recently acquired by the core and has therefore been at high density for shorter time than the rest (i.e., it is “younger” and less depleted, see also Kuiper et al. 1996). A peculiar velocity in this material is exactly what would have been expected if this interpretation is correct.

## 4. Discussion

### 4.1. Core structure and equilibrium state

We have seen that the systematic internal motions in both L1498 and L1517B are of the order of  $0.1 \text{ km s}^{-1}$  and therefore subsonic for gas at  $10 \text{ K}$  (sound speed is  $0.19 \text{ km s}^{-1}$ ). This suggests that both cores are close to a state of hydrostatic equilibrium in which the core self gravity is balanced by internal forces. Given the core parameters we have derived in previous sections, we now analyze whether such an equilibrium state is possible and whether it is consistent with the observed core structure.

The simplest support component in each core is the thermal pressure  $P_T = nkT$ , where  $n$  is the gas density,  $k$  is the Boltzmann constant, and  $T$  the gas kinetic temperature. This pressure may be supplemented by a non-thermal component  $P_{NT} = mn\sigma_{NT}^2$  if the non-thermal linewidth arises from turbulent supporting motions ( $m$  is the mean particle mass and  $\sigma_{NT}$  is the non thermal velocity dispersion, related to the non thermal FWHM by  $\Delta V_{NT} = \sqrt{8 \ln 2} \sigma_{NT}$ ). The relative importance of these two supporting components is given by the ratio  $P_{NT}/P_T = \sigma_{NT}^2/(kT/m)$ , which can be easily estimated from the core parameters derived in previous sections. As both  $\sigma_{NT}$  and  $T$  are constant over the central  $0.1 \text{ pc}$  of L1498 and L1517B, the pressure ratio is constant, and has a value of  $0.07$  for  $\Delta V_{NT} = 0.12 \text{ km s}^{-1}$  and  $T = 10 \text{ K}$  (Sections 3.3 and 3.7.1). This low ratio indicates that the non thermal motions contribute negligibly to the core support over at least the central  $0.1 \text{ pc}$  (see also Fuller & Myers 1993), and that in the absence of support by an ordered magnetic field, thermal pressure is the main supporting agent in both L1498 and L1517B (a similar conclusion for the case of B68 has been recently obtained by Lada et al. 2003).

If thermal pressure dominates core support and the gas temperature is constant, the equation of core hydrostatic equilibrium reduces to the isothermal case, which has a classical solution for spherical geometry (Chandrasekhar 1939). The addition of a constant non-thermal contribution implies only a simple generalization of the isothermal case and does not change the solution significantly (e.g., Appendix A of McLaughlin & Pudritz 1996). As

we have seen in section 3.1, the density profiles derived from the dust continuum emission do in fact have *shapes* very close to those expected for isothermal spheres, especially in the case of L1517B. To check whether these profiles are consistent with equilibrium between self gravity and internal (thermal plus non thermal) pressure, we can compare the measured velocity dispersion  $\sigma$  ( $=0.185 \text{ km s}^{-1}$  for gas at  $9.5 \text{ K}$  and  $\Delta V_{NT} = 0.11 \text{ km s}^{-1}$ ) with the velocity dispersion required by the isothermal fit to the dust emission (section 3.1). Unfortunately, the fit only constrains the combined parameter  $\sigma\sqrt{\kappa_\nu B(T_d)}$ , making impossible a full check without independent estimates of the dust emissivity  $\kappa_\nu$  and temperature  $T_d$ .<sup>1</sup> To take into account this dependence, we re-write the velocity dispersions required from the continuum fits in Table 1 (where we assumed  $\kappa_\nu = 0.005 \text{ cm}^2 \text{ g}^{-1}$  and  $T_d = 10 \text{ K}$ ) as  $\sigma = 0.27 (\kappa_\nu/0.005)^{-0.5} (B(T_d)/B(10))^{-0.5} \text{ km s}^{-1}$  for L1517B and  $0.32 (\kappa_\nu/0.005)^{-0.5} (B(T_d)/B(10))^{-0.5} \text{ km s}^{-1}$  for L1498. These values show that if  $\kappa_\nu = 0.005 \text{ cm}^2 \text{ g}^{-1}$  and  $T_d = 10 \text{ K}$ , there is either an extra pressure contribution which does not affect the observed linewidth or the cores should be contracting under their own gravity.

Although a state of slow contraction is likely in both L1498 and L1517B (section 3.7.2), we cannot rule out that at least part of the velocity dispersion mismatch reflects a wrong choice of dust parameters. For example, the value of  $T_d = 10 \text{ K}$ , chosen so it equals the well-measured gas temperature, may in fact be a slight overestimate. This is suggested by the models of Galli et al. (2002) (their Fig.3), which show that although dust and gas are thermally coupled at core densities the dust is cooler by about  $2 \text{ K}$ . A lower dust temperature requires a larger  $\sigma$ , and this makes the pressure unbalance more severe, although only by a small margin: a dust temperature of  $8 \text{ K}$  requires a 1.2 increase in  $\sigma$ . More critical in the balance argument is the choice of the dust emissivity  $\kappa_\nu$ , as this parameter is considered to be uncertain by a factor of 2. In L1517B, for example, if  $\kappa_\nu = 0.01 \text{ cm}^2 \text{ g}^{-1}$ , the gas will be in hydrostatic equilibrium assuming  $T_d = 10 \text{ K}$ . This higher  $\kappa_\nu$  value is not too far from the  $0.008 \text{ cm}^2 \text{ g}^{-1}$  recommended by Ossenkopf & Henning (1994) for a standard gas-to-dust ratio of 100 and dust in regions of density  $\approx 10^5 \text{ cm}^{-3}$ , which is typical of the L1517B center, and recent observations do in fact suggest a systematic increase of  $\kappa_\nu$  at high densities (Kramer et al. 2003; Bianchi et al. 2003). Thus, it is still possible that L1517B is exactly or very close to a state of hydrostatic equilibrium where its (mostly thermal) pressure balances its self gravity. This higher  $\kappa_\nu$  value, however, will not bring L1498 to a state

<sup>1</sup> The parameters directly derived from fitting the radial distribution of dust emission with an isothermal model (including an on-the-fly simulation) are the King radius  $r_K = \sqrt{9\sigma^2/4\pi G\rho_0}$  (from the shape of the profile) and the central emissivity  $j_\nu = \kappa_\nu \rho_0 B(T_d)$  (from the intensity scale), where  $\rho_0$  is the central density and  $T_d$  the dust temperature. Substituting  $\rho_0$  from the second equation into the first one, we obtain  $\sigma\sqrt{\kappa_\nu B(T_d)}$ .

of equilibrium, and this is also consistent with the non spherical shape of this core.

#### 4.2. Core chemistry and comparison with models

The abundance profiles of  $\text{NH}_3$ ,  $\text{N}_2\text{H}^+$ , and the isotopomers of CO and CS can be qualitatively understood as the result of the selective freeze out of molecules onto cold dust grains as the gas becomes centrally concentrated during core formation. The lower binding energy of  $\text{N}_2$  to grain surfaces makes this species relatively overabundant at high densities, and this in turn favors the presence of molecules composed of N and H (like  $\text{NH}_3$  and  $\text{N}_2\text{H}^+$ ) in the core interiors. This selective freeze out of molecules during core contraction and its resulting chemistry has been modeled in detail by a number of authors over the last few years (Bergin & Langer 1997; Charnley 1997; Caselli et al. 1999; Nejad & Wagenblast 1999; Aikawa et al. 2001; Li et al. 2002; Shematovich et al. 2003; Aikawa et al. 2003), and their results are in general agreement with the observations and analysis presented here. A detailed comparison between models and data, however, reveals some differences between observed molecular behavior and theoretical expectations, and in this section we comment on the possible origin of these differences.

The main disagreement between our observations and the published models involves the behavior of  $\text{NH}_3$  and  $\text{N}_2\text{H}^+$  near the core centers. As seen in sections 3.3 and 3.4, both L1498 and L1517B present the same pattern of constant  $\text{N}_2\text{H}^+$  abundance together with a factor-of-a-few central  $\text{NH}_3$  increase, and this pattern seems also present in other starless cores (see TMCWC). Most chemical models, however, predict that  $\text{NH}_3$  and  $\text{N}_2\text{H}^+$  will behave in a similar fashion given that they have  $\text{N}_2$  as a common parent. This is qualitatively correct in that the two species trace the same regions but the quantitative differences noted above require explanation. Aikawa et al. (2003) have made a detailed attempt to fit observations of L1544 (their Fig. 8). Their best model (a delayed collapse with N initially molecular and a high CO binding energy) has an essentially constant  $\text{NH}_3/\text{N}_2\text{H}^+$  abundance ratio as a function of radius.

It is unclear which processes cause the  $\text{NH}_3$  and  $\text{N}_2\text{H}^+$  abundances to follow different trends at high densities and produce the relative enhancement of  $\text{NH}_3$ . Both have their origins in molecular nitrogen and hence their abundance ratio should be independent of the  $\text{N}_2$  abundance. Their formation involves reactions with  $\text{He}^+$  (in the case of  $\text{NH}_3$ ) and  $\text{H}_3^+$  (in the case of  $\text{N}_2\text{H}^+$ ) and thus their abundance ratio is sensitive to the abundance ratio of these ions. The ionic abundances are certainly sensitive to the depletion of CO and other molecules and hence uncertainties in key rates determining the abundances of  $\text{He}^+$  and  $\text{H}_3^+$  may be responsible for variations in the  $\text{NH}_3/\text{N}_2\text{H}^+$  abundance ratio. Apart from this, we note that while  $\text{N}_2\text{H}^+$  is likely mainly destroyed by recombination with electrons

and reactions with CO, it is rather unclear what the main destruction mechanism for NH<sub>3</sub> is in regions where CO (and hence carbon compounds in general) is sufficiently depleted that reactions with ions such as C<sup>+</sup> become negligible. The answers to these questions may provide the explanation for the observed gradient in the NH<sub>3</sub>/N<sub>2</sub>H<sup>+</sup> ratio.

#### 4.3. Core formation

Although it is clear that dense cores contract from the lower density gas of their surrounding molecular clouds, how this process occurs and how long it takes is still a matter of much uncertainty (see, e.g., Shu et al. 1987 and Hartmann et al. 2001 for two opposing views). This state of affairs results in part because it is not yet possible to infer a core contraction history directly from observations, as we lack reliable time markers to assess the evolutionary state of different cores. Fortunately, the time and density dependence of the freeze out process may offer the possibility of shedding some light on the core contraction history by allowing us to correlate the molecular abundances of volatile species with the evolutionary state of the gas in a core. Here we present a first (and preliminary) application of these ideas to the case of the L1498 and L1517B cores.

Both L1498 and L1517B appear highly symmetric in their distribution of N<sub>2</sub>H<sup>+</sup>, NH<sub>3</sub>, and dust continuum (Fig. 3), which are the most reliable tracers of the dense core gas. L1498, especially in the density-sensitive N<sub>2</sub>H<sup>+</sup>, presents an evident bilateral symmetry with respect to a NE-SW axis, and L1517B has an almost perfect circular symmetry with only minor deviations. These symmetries in the emission of the most robust tracers most likely reflect a high degree of symmetry in the underlying distributions of matter in the cores, in agreement with their state close to hydrostatic equilibrium.

In contrast with the symmetric distributions of N<sub>2</sub>H<sup>+</sup>, NH<sub>3</sub>, and dust continuum, the distributions of CS and CO emission in L1498 and L1517B are highly asymmetric (Fig. 3). As we have seen in sections 3.5 and 3.6, these asymmetries arise from a pattern of non axisymmetric abundance variations that is superposed to the central abundance drop due to molecular freeze out. These non axisymmetric variations are located at radii where freeze out is already prevalent, so they very likely represent variations in the amount of freeze out, in the sense that the bright spots to the SE and E of L1498 and to the W of L1517B are places where this process is less severe and therefore the CO and CS abundances are higher. This interpretation is supported by the fact that the same regions have at the same time bright CO, CS, and other molecules that freeze out at similar densities (Tafalla et al. 2004 in preparation), indicating that the process responsible for the asymmetry is not limited to one particular chemical species.

As molecular freeze out is very sensitive to the time the gas has spent at high density (e.g., Bergin & Langer 1997), the simplest explanation of the lower freeze out at

the CO and CS bright spots is that these regions have somehow stayed at high density less time than other regions with similar radius (and therefore similar present density). (Pre-existing chemical inhomogeneities seem unlikely because of the small scale.) For this to happen, the contraction of the gas in L1498 and L1517B has to have been non spherically symmetric, with the gas at the CO and CS bright spots being “younger” (less processed) and therefore more recently accreted. This interpretation is consistent with the correlation between enhanced CO/CS abundance and “high” velocity N<sub>2</sub>H<sup>+</sup> and NH<sub>3</sub> found in section 3.7.2 (see Fig. 13), as the younger portions of the core will have not yet attained perfect equilibrium and thus retain a fraction of their contraction speed. Kinematics and chemical composition, therefore, agree in suggesting that L1498 and L1517B have formed from non spherical contraction of cloud material. The time scale of this contraction seems to be of the order of a few Myr (section 3.7.2).

The above time scale, although short, is not enough to discriminate between the different scenarios of star formation. On the one hand, the value is consistent with a picture of relatively rapid star formation (Elmegreen 2000; Hartmann et al. 2001), but on the other, it is also consistent with ambipolar diffusion models that start with an initially not highly subcritical cloud (Li 1999; Ciolek & Basu 2001). In paper 2, we will revisit the time scale issue based on the analysis of the freeze out process of a large number of molecular species. Here we note that if the magnetically-mediated scenario is correct, the fastest gas motions are expected to occur along the magnetic field axis, and this would imply a correlation of the observed abundance anisotropies with the magnetic field direction. Observations of the polarization direction in the submillimeter continuum should be able to test this prediction.

More conclusive than the kinematic estimate of the contraction time scale is the measurement of the (low) turbulence level inside the cores. Our observations of L1498 and L1517B (Fig. 10, top) appear to be inconsistent with typical expectations from the supersonic turbulence scenario (see Mac Low & Klessen 2003 for a recent review). Ballesteros-Paredes et al. (2003) have recently argued that density profiles similar to those of hydrostatic equilibrium systems can appear fortuitously in model simulations of supersonic turbulence, showing that the shape of the density profile is not a reliable indication of a core equilibrium state. Although it is true that the cores in the Ballesteros-Paredes et al. (2003) simulations can mimic the density profiles of systems like L1498 and L1517B, their internal velocity fields clearly betray their “hydrostatic disguise.” Turbulent model cores in the simulations of Ballesteros-Paredes et al. (2003) present velocity profiles with internal changes larger than the speed of sound, and on the order of 0.5-1 km s<sup>-1</sup> in cases of driven turbulence (their Figs. 9-11). Our observations rule out such strong velocity changes by about an order of magnitude, and not only in the plane of the sky (from our radial profiles of line center velocity, see Fig. 11), but also along any

given line of sight (our linewidth measurements, see Fig. 10).

The problem of the supersonic turbulence scenario is unlikely to be restricted to L1498 and L1517B, as these objects seem representative of the Taurus core population in, for example, having narrow lines (e.g., Fuller & Myers 1993). This problem points to the need of any model of core formation for producing condensations which appear thermally dominated and extremely quiescent. How these close to hydrostatic equilibrium configurations can be achieved in the relatively short time of a few Myr seems to pose a challenge to most core formation models.

## 5. Conclusions

We have presented detailed models of the internal structure of two close-to-round starless cores in the nearby Taurus-Auriga star formation complex, L1498 and L1517B. Our models have been constrained from the simultaneous fit of the spatial distribution and the central emerging spectrum of at least two transitions of  $\text{NH}_3$ ,  $\text{N}_2\text{H}^+$ , CS,  $\text{C}^{34}\text{S}$ ,  $\text{C}^{18}\text{O}$ , and  $\text{C}^{17}\text{O}$ , together with maps of the 1.2 mm continuum. The main conclusions of this work are:

1. Both cores present gas temperature distributions consistent with a constant value (10 K for L1498 and 9.5 K for L1517B) and a very small rms (1 K). No evidence for radial temperature gradients is found in the central 0.1 pc.

2. Assuming constant dust temperature and emissivity, we derive density profiles for both L1498 and L1517B of the form  $n(r) = n_0/(1 + (r/r_0)^\alpha)$ , where  $n_0$ ,  $r_0$ , and  $\alpha$  are free parameters. For L1517B, the  $\alpha = 2.5$  best fit is indistinguishable from an isothermal sphere fit, and for L1498 the  $\alpha = 3.5$  best fit is close to the isothermal fit.

3. From the combination of radiative transfer modeling and hyperfine fitting of the  $\text{NH}_3$  and  $\text{N}_2\text{H}^+$  spectra, we determine that in both L1498 and L1517B the non thermal component of the linewidth is constant with radius over at least the central 0.1 pc. This component is smaller than the thermal linewidth and has a FWHM of about 0.12  $\text{km s}^{-1}$  in both cores. Its scatter in the radial profiles is extremely small (< 5%), and it is consistent with the measurement uncertainty.

4. Using a Monte Carlo radiative transfer code and the radial profiles of density, temperature, and linewidth, we determine radial profiles of molecular abundance for all observed species. For  $\text{NH}_3$ , the abundance at the core centers is a factor of a few higher than at intermediate radii (0.05 pc). For  $\text{N}_2\text{H}^+$ , a constant abundance model fits well the emission at all radii in L1517B, while a drop by a factor of 3 at large radii is preferred in L1498. For both CO and CS (and isotopomers), constant abundance models fail dramatically to fit the emission, and an abrupt central abundance drop is needed to explain the data. The abundance drop of these two species is so severe that the emission can be modeled with step functions and no molecules at the center.

5. The central abundance drop of CO and CS seems to arise from the freeze out of these molecules onto cold dust grains at densities of a few  $10^4 \text{ cm}^{-3}$ . The simultaneous survival of  $\text{N}_2\text{H}^+$  and  $\text{NH}_3$  seems related to the lower binding energy to grains of  $\text{N}_2$ , which allows the production of these two species at the core centers. The relative increase of the  $\text{NH}_3$  abundance over  $\text{N}_2\text{H}^+$  probably results from a combination of a more efficient  $\text{NH}_3$  production in the highly CO-depleted core interiors and a decrease in the ion fraction with density, although further modeling is required to understand this behavior.

6. Superposed to the pattern of radial abundance gradients there is a weaker pattern of non axially symmetric abundance variations in both CO and CS. This pattern results from asymmetries in the distribution of CO and CS freeze out, and its presence indicates that the process responsible for the freeze out has not been spherically symmetric. As gas contraction to form the cores is the likely cause of the central freeze out, the asymmetry suggests that core formation has occurred in a non spherically symmetric way.

7. The analysis of the line center velocities of the freeze-out resistant  $\text{N}_2\text{H}^+$  and  $\text{NH}_3$  reveals spatial variations at the level of 0.1  $\text{km s}^{-1}$  in both L1498 and L1517B. The spatial distribution of these variations is complex and cannot be explained with a simple pattern like rotation. It most likely represents internal bulk motions in the core gas. Some gas at anomalous velocities has a spatial distribution similar to the gas with anomalously high CO and CS abundance in the pattern of non axisymmetric freeze out. This similarity suggests that part of the observed bulk motions result from residual core contraction. If so, the contraction time is of the order of 1 Myr.

8. We have used the model physical parameters to study the stability of L1498 and L1517B. The small non thermal linewidth indicates that any turbulent pressure support is negligible in both cores (< 10 %), and that in the absence of magnetic fields, thermal pressure is the only stabilizing agent. Although the density profiles have the shape expected for isothermal equilibrium, the mass estimated from the continuum is larger than what could be held in equilibrium. Either our choice of dust parameters is incorrect, there is additional magnetic support, or the cores are in state of (slow) contraction. In any case, the observed velocity and linewidth profiles in both L1498 and L1517B are inconsistent with representative predictions of supersonic turbulence models that generate density profiles similar to those of an isothermal sphere.

*Acknowledgements.* We thank the IRAM 30m staff for help during the observations, Carl Gottlieb for communicating new frequency measurements prior to publication, Daniele Galli for providing us with model gas temperature profiles for L1517B, Zhi-Yun Li for advise on ambipolar diffusion models, and Alexander Lapinov for bringing to our attention recent work on approximations to the isothermal sphere. We also thank the referee, Ted Bergin, for comments that helped clarifying the manuscript. MT acknowledges partial support from grant AYA2000-0927 of the Spanish DGES. PC and CMW acknowl-

edge support from the MIUR project “Dust and Molecules in Astrophysical Environments.” This research has made use of NASA’s Astrophysics Data System Bibliographic Services and the SIMBAD database, operated at CDS, Strasbourg, France.

## Appendix A: A simple analytic approximation to the isothermal sphere

In TMCWC we fitted the volume density profiles of 5 dense cores using an analytical expression of the form

$$n(r) = \frac{n_0}{1 + (r/r_0)^\alpha},$$

with  $n_0$ ,  $r_0$ , and  $\alpha$  as free parameters. The motivation of this choice was purely empirical, based on the ability of these profiles to fit the observed radial distribution of dust continuum emission. A later hydrostatic equilibrium analysis of these profiles (unpublished) showed that for  $\alpha = 2.5$  an almost perfect balance between isothermal plus constant turbulence pressure and self gravity was achieved. Intrigued by this “coincidence,” especially because an  $\alpha = 2.5$  profile lacks the proper asymptotic behavior for an isothermal sphere ( $1/r^2$ ), we carried out a point-by-point comparison between this profile and the numerical solution of the isothermal function given by Chandrasekhar & Wares (1949). These authors calculated numerically the mass density profile for an isothermal sphere normalized to the central density ( $\rho_0$ ), which can be written as  $\rho = \exp(-\psi)$  with  $\psi$  being the solution of

$$\frac{1}{\xi^2} \frac{d}{d\xi} \left( \xi^2 \frac{d\psi}{d\xi} \right) = e^{-\psi},$$

and  $\xi = \sqrt{4\pi G\rho_0/\sigma^2} r$  (see Chandrasekhar 1939 for a full discussion). To compare our  $\alpha = 2.5$  profile with this function, we normalize it and require that it reaches the half maximum density at the same radius as the isothermal solution ( $\xi \approx 2.25$ ), and this completely fixes the profile as

$$\rho_{app}(\xi) = \frac{1}{1 + (\xi/2.25)^{2.5}}$$

Fig. A1 shows (top) a comparison between the  $\alpha = 2.5$  profile and the numerical solution from Chandrasekhar & Wares (1949). For additional comparison, we also present the classical modified Hubble law approximation (Binney & Tremaine 1987) and the recent simple approximation proposed by Natarajan & Lynden-Bell (1997) (their case b). As can be seen, the  $\alpha = 2.5$  profile remains within 10% from the exact solution up to a larger  $\xi$  value than the other solutions (although the Natarajan & Lynden-Bell (1997) profile finally converges to the exact solution for large  $\xi$ ). In fact, the  $\alpha = 2.5$  solution is accurate within 10% for  $\xi \leq 23$ , more than 3.5 times the instability radius (Ebert 1955; Bonnor 1956), and over this range, the density varies by more than a factor 300. The associated instability point of this solution ( $\xi = 6.467$ ) is within 0.25% of the exact solution ( $\xi = 6.451$ , Hunter 1977). This shows that the  $\alpha = 2.5$  profile can be used to approximate any stable Bonnor-Ebert sphere within 10%.

## Appendix B: Kinetic temperature estimate from NH<sub>3</sub>

The lack of allowed radiative transitions between the (J,K)=(2,2) and (1,1) levels of NH<sub>3</sub> makes their relative population (described by the rotational temperature  $T_R^{21}$ ) highly

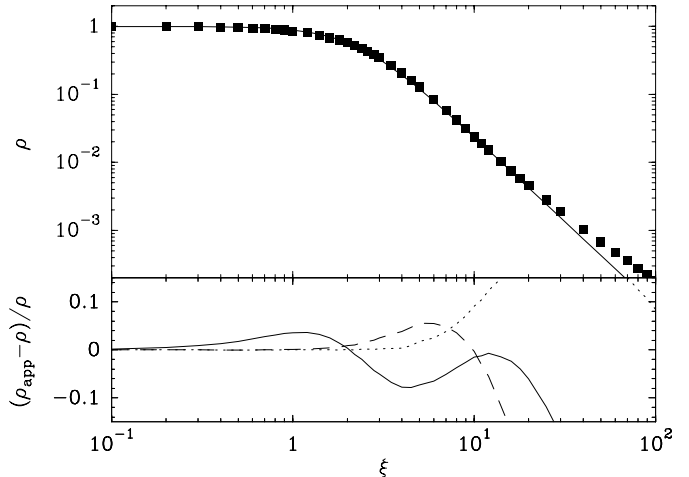


**Fig. A.1.** Top: Numerical solution of the isothermal function from Chandrasekhar & Wares (1949) (squares) compared to our simple  $\alpha = 2.5$  analytic model (line). Bottom: relative error of several analytic approximations to the isothermal sphere. The solid line represents the  $\alpha = 2.5$  profile presented here, the long-dashed lines is the modified Hubble law, and the dotted line is model b from Natarajan & Lynden-Bell (1997). Note how the  $\alpha = 2.5$  profile remains within 10% of the exact solution to higher  $\xi$  values than the other profiles (although it finally diverges while the Natarajan & Lynden-Bell (1997) curve converges to the right solution at large  $\xi$ ).

sensitive to collisions, and therefore a good estimator of the gas kinetic temperature. In the traditional NH<sub>3</sub> analysis, the (1,1) and (2,2) populations are calculated from the spectra assuming LTE conditions, and the derived  $T_R^{21}$  rotational temperature is converted into an estimate of the gas kinetic temperature  $T_K$  (Walmsley & Ungerechts 1983). To test this procedure and to calibrate the  $T_R^{21}$ - $T_K$  relation using realistic radiative transfer and cloud conditions, we have run a series of Monte Carlo models and produced synthetic (1,1) and (2,2) spectra. These spectra have been analyzed using the standard NH<sub>3</sub> procedure, and the derived gas parameters have been compared with those used in the models.

Our NH<sub>3</sub> Monte Carlo model has been described in TMCWC and is based on that of Bernes (1979), adapted to handle NH<sub>3</sub>. It includes the 6 lowest levels of para-NH<sub>3</sub>, which contain more than 99.9% of the molecules at 10 K (typical core gas temperature). It assumes that the relative hf sub-populations of the meta-stable levels are in LTE (as required by observations), and calculates the relative populations between the (1,1), (2,1), and (2,2) levels in a self-consistent manner. It uses the collision coefficients with H<sub>2</sub> of Danby et al. (1988), which seems to be the most accurate set available, according to recent laboratory measurements (Willey et al. 2002). As cloud parameters, we use the density profiles derived from dust emission for L1498 (*L1498-models*) and L1517B (*L1517B-models*), and assume a constant gas temperature (given the results of section 3.3), which we have varied from 5 to 20 K.

In all 9 models we have run we find that while both the (1,1) and (2,2) excitation temperatures vary with radius by a factor of several (as a result of the core density gradient), the  $T_R^{21}$  rotational temperature stays constant over the core within

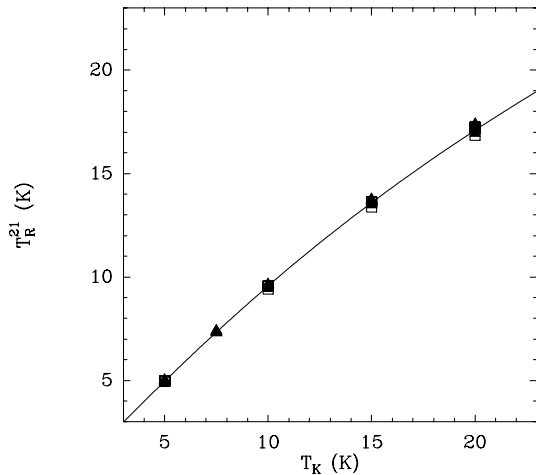


**Fig. B.1.**  $T_R^{21}$  versus  $T_K$  derived using Monte Carlo models.  $T_K$  is the (constant) gas kinetic temperature and  $T_R^{21}$  is the (2,2)-to-(1,1) rotation temperature derived by applying the standard  $\text{NH}_3$  analysis to the Monte Carlo spectra. Filled triangles and open squares represent models having the analytic density profile derived in section 3.1 for L1517B and L1498, respectively (see Table 2). Multiple points at the same  $T_K$  represent values measured at radii equal 0, 10, 30, 60, 100, and 150 arcseconds (data convolved to the 40'' resolution of the Effelsberg 100m telescope). The solid line is the analytic expression proposed in the text to derive  $T_K$  using the  $T_R^{21}$  estimate from the standard  $\text{NH}_3$  analysis.

2% or less. This makes the derivation of  $T_R^{21}$  using the standard  $\text{NH}_3$  analysis (e.g., Bachiller et al. 1987) rather accurate, despite of violating one of its basic assumptions: that of a single excitation temperature for both (1,1) and (2,2). In fact, our models show that in the range of kinetic temperatures we have explored (5-20 K),  $T_R^{21}$  estimates using the standard analysis agree within 5% with the real values, and that the agreement is at the 1% level for temperatures around 10 K or lower. Thus,  $T_R^{21}$  can be easily and accurately determined from observations for realistic core conditions.

The critical part of the  $\text{NH}_3$  analysis is the conversion of the  $T_R^{21}$  estimate into an estimate of the gas kinetic temperature  $T_K$ , as this step requires a full solution of the radiative transfer equation. Walmsley & Ungerechts (1983) have presented a simple analytic expression derived under simplifying assumptions and using an old version of the  $\text{NH}_3$ - $\text{H}_2$  collision coefficients from Green (1981). In order to derive a revised expression using realistic radiative transport and the new collision coefficients of Danby et al. (1988), we compare the  $T_K$  inputs in the Monte Carlo models with the  $T_R^{21}$  values derived from the above analysis. As can be seen in Figure B.1., for any given  $T_K$  between 5 and 20K, the L1498-models and L1517B-models predict the same  $T_R^{21}$  within 5% or better, and this shows that at least for our conditions, the  $T_R^{21}$ - $T_K$  relation is almost independent of the details of core density, size, etc. To derive an analytic expression for this relation, we use as inspiration equation 2 of Walmsley & Ungerechts (1983), although we look for the inverse function of theirs because we want to predict  $T_K$  given the  $T_R^{21}$  value determined with the standard  $\text{NH}_3$  analysis. After some experimentation, we have found that

the following expression

$$T_K = \frac{T_R^{21}}{1 - \frac{T_R^{21}}{42} \ln[1 + 1.1 \exp(-16/T_R^{21})]}$$

fits the points in the range  $T_K = 5$ -20 K to better than 5%, and therefore provides an accurate gas temperature estimate based on easy-to-measure quantities. We recommend this relation to derive  $T_K$  in dense, cold cores at temperatures lower than or around 20 K (extrapolation to higher temperatures requires further modeling).

## References

Aikawa, Y., Ohashi, N., Inutsuka, S., Herbst, E., & Takakuwa, S. 2001, ApJ, 552, 639  
 Aikawa, Y., Ohashi, N., & Herbst, E. ApJ, 593, 906  
 Alves, J., Lada, C.J., Lada, E.A. 1999, ApJ, 515, 265  
 Alves, J., Lada, C.J., Lada, E.A. 2001, Nat, 409, 159  
 André, P., Ward-Thompson, D., & Motte, F. 1996, A&A, 314, 625  
 Bachiller, R., Guilloteau, S., & Kahane, C. 1987, A&A, 173, 324  
 Bacmann, A., André, P., Puget, J.-L., Abergel, A., Bontemps, S., & Ward-Thompson, D. 2000, A&A, 361, 558  
 Bacmann, A., Lefloch, B., Ceccarelli, C., Castets, A., Steinacker, J., & Loinard, L. 2002, A&A, 389, L6  
 Ballesteros-Paredes, J., Klessen, R.S., & Vázquez-Semadeni, E. 2003, ApJ, 592, 188  
 Barranco, J.A., & Goodman, A.A. 1998, ApJ, 504, 207  
 Beichman, C.A., Myers, P.C., Emerson, J.P., Harris, S., Mathieu, R., Benson, P.J., & Jennings, R.E. 1986, ApJ, 307, 337  
 Bergin, E.A., & Langer, W.D. 1997, ApJ, 486, 316  
 Bergin, E.A., Ciardi, D.R., Lada, C.J., Alves, J., Lada, E.A. 2001, ApJ, 557, 209  
 Bergin, E.A., Alves, J., Huard, T., & Lada, C.J. 2002, ApJ, 570, L101  
 Bernes, C. 1979, A&A, 73, 67  
 Benson, P.J., & Myers, P.C. 1989, ApJS, 71, 89  
 Bianchi, S., Gonçalves, J., Albrecht, M., Caselli, P., Chini, R., Galli, D., & Walmsley, M. 2003, A&A, 399, L43  
 Binney, J., & Tremaine, S. (1987) Galactic Dynamics (Princeton University Press, Princeton)  
 Bonnor, W.B. 1956, MNRAS, 116, 351  
 Broguière, D., Neri, R., & Sievers, A. 1996, IRAM Tech. Report.  
 Caselli, P., Myers, P.C., & Thaddeus, P. 1995, ApJ, 455, L77  
 Caselli, P., Walmsley, C.M., Tafalla, M., Dore, L., Myers, P.C. 1999, ApJ, 523, L165  
 Caselli, P., Benson, P.J., Myers, P.C., & Tafalla, M. 2002a, ApJ, 572, 238  
 Caselli, P., Walmsley, C.M., Zucconi, A., Tafalla, M., Dore, L., & Myers, P.C. 2002, ApJ, 565, 344  
 Caselli, P., Walmsley, C.M., Zucconi, A., Tafalla, M., Dore, L., & Myers, P.C. 2002, ApJ, 565, 331  
 Cazzoli, G., Dore, L., Puzzarini, C., & Beninati, S. 2002, Phys. Chem. Chem. Phys., 4, 3575  
 Chandrasekhar, S. 1939, An Introduction to the Study of Stellar Structure (Univ. Chicago Press, Chicago)  
 Chandrasekhar, S., & Wares, G.W. 1949, ApJ, 109, 551  
 Charnley, S.B. 1997, MNRAS, 291, 455  
 Ciolek, G.E. & Basu, S. 2001, ApJ, 547, 272

Curry, C. 2002, *ApJ*, 576, 849

Danby, G., Flower, D.R., Valiron, P., Schilke, P., & Walmsley, C.M. 1988, *MNRAS*, 235, 229

Ebert, R. 1956, *Z. Astrophys.*, 37, 216

Elmegreen, B.G. 1979, *ApJ*, 232, 729

Elmegreen, B.G. 2000, *ApJ*, 530, 277

Evans, N.J. II 1999, *ARA&A*, 37, 311

Evans, N.J.II, Rawlings, J.M.C., Shirley, Y.L., Mundy, L.G. 2001, *ApJ*, 557, 193

Flower, D.R. 1999, *MNRAS*, 305, 651

Fuller, G.A., & Myers, P.C. 1993, *ApJ*, 418, 273

Galli, D. Walmsley, M. Gonçalves, J. 2002, *A&A*, 394, 275

Goldsmith, P.F. 2001, *ApJ*, 557, 736

Goodman, A.A., Benson, P.J., Fuller, G.A., & Myers, P.C. 1993, *ApJ*, 406, 528

Goodman, A.A., Barranco, J.A., Wilner, D.J., & Heyer, M.H. 1998, *ApJ*, 504, 223

Gottlieb, C.A., Myers, P.C., & Theddeus, P. 2003, *ApJ*, 588, 655

Green, S. 1981, NASA Tech. Memo. 83869

Hartmann, L., Ballesteros-Paredes, J., & Bergin, E. 2001, *ApJ*, 562, 852

Hotzel, S., Harju, J., & Juvela, M. 2002, *A&A*, 395, L5

Houde, M., Bastien, P., Peng, R., Phillips, T.G., & Yoshida, H. 2000, *ApJ*, 536, 857

Hunter, C. 1977, *ApJ*, 218, 834

Jessop, N.E., & Ward-Thompson, D. 2001, *MNRAS*, 323, 1025

Jones, C.E. & Basu, S. 2002, *ApJ*, 569, 280

Kramer, C., Alves, J., Lada, C.J., Lada, E.A., Sievers, A., Ungerechts, & Walmsley, C.M. 1999, *A&A*, 342, 257

Kramer, C., Richer, J., Mookerjea, B., Alves, J., & Lada, C. 2003, *ApJ*, 399, 1073

Kreysa, E., et al. 1998, *SPIE*, 3357, 319

Kukolich, S.G. 1966, *Phys. Rev.*, 156, 83

Kuiper, T.B.H., Langer, W.D., & Velusamy, T. 1996, *ApJ*, 468, 761

Lada, C.J., Bergin, E.A., Alves, J.F., & Huard, T.R. 2003, *ApJ*, 586, 286

Langer, W.D., & Willacy, K. 2001, *ApJ*, 557, 714

Lee, C.W. & Myers, P.C. 1999, *ApJS*, 123, 233

Lee, C.W., Myers, P.C., Tafalla, M. 1999, *ApJ*, 526, 788

Lee, C.W., Myers, P.C., Tafalla, M. 2001, *ApJS*, 136, 703

Lemme, C., Walmsley, C.M., Wilson, T.L., & Muders, D. 1995 *A&A*, 302, 509

Levin, S.M., Langer, W.D., Velusamy, T., Kuiper, T.B.H., Crutcher, R.M. 2001, *ApJ*, 555, 850

Li, Z.-Y. 1999, *ApJ*, 526, 806

Li, Z.-Y., Shematovich, V.I., Wiebe, D.S., Shustov, B.M. 2002, *ApJ*, 569, 792

Lucas, R., & Liszt, H. 1998, *A&A*, 337, 246

Mac Low, M.-M. & Klessen, R.S. 2003, *Rev. Mod. Phys.*, submitted (astro-ph/0301093)

Mathis, J.S., Mezger, P.G., & Panagia, N. 1983, *A&A*, 128, 212

McCall, B.J. et al. 2003, *Nat.* 422, 500

McLaughlin, D.E., & Pudritz, R.E. 1996, *ApJ*, 469, 194

Müller, H.S.P., Thorwirth, S., Roth, D.A., & Winnewisser, G. 2001, *A&A*, 370, L49

Myers, P.C. 1983, *ApJ*, 270, 105

Myers, P.C., Linke, R.A., & Benson, P.J. 1983, *ApJ*, 264, 517

Myers, P.C. 1999, in *The Physics and Chemistry of the Interstellar Medium*, eds. V. Ossenkopf, J. Stutzki, and G. Winnewisser, (Herdecke: GCA-Verlag), 227

Myers, P.C., Fuller, G.A., Mathieu, R.D., Beichman, C.A., Benson, P.J., Schild, R.E., & Emerson, J.P. 1987, *ApJ*, 319, 340

Natarajan, P., & Lynden-Bell, D. 1997, *MNRAS*, 286, 268

Nejad, L.A.M., & Wagenblast, R. 1999, *A&A*, 350, 204

Ossenkopf, V., & Henning, T. 1994, *A&A*, 291, 943

Penzias, A.A. 1981, *ApJ*, 249, 518

Shematovich, V.I., Wiebe, D.S., Shustov, B.M., Li, Z.-Y. 2003, *ApJ*, 588, 894

Shu, F.H., Adams, F.C., & Lizano S. 1987, *ARA&A*, 25, 23

Tafalla, M., Mardones, D., Myers, P.C. Caselli, P., Bachiller, R., & Benson, P.J. 1998, *ApJ*, 504, 900

Tafalla, M., Myers, P.C. Caselli, P., Walmsley, C.M., & Comito, C. 2002, *ApJ*, 569, 815

Walmsley, C.M., & Ungerechts, H. 1983, *A&A*, 122, 164

Ward-Thompson, D., André, P., & Kirk, J.M. 2002, *MNRAS*, 329, 257

Ward-Thompson, D., Scott, P.F., Hills, R.E., & André, P. 1994, *MNRAS*, 268, 276

Willacy, K., Langer, W.D., & Velusamy, T. 1998, *ApJ*, 507, L171

Willey, D.R., Timlin, R.E., Merlin, J.M., Sowa, M.M., & Wesolek, D.M. 2002, *ApJS*, 139, 191

Wolkovitch, D., Langer, W.D., Goldsmith, P.F., & Heyer, M. 1997, *ApJ*, 477, 241

Zhou, S., Wu, Y., Evans, N.J.II, Fuller, G.A., & Myers, P.C. 1989, *ApJ*, 346, 168

Zucconi, A., Walmsley, C.M., & Galli, D. 2001, *A&A*, 376, 650